Gap Junctions Contribute to Differential Light Adaptation across Direction-Selective Retinal Ganglion Cells

Highlights

- At low light levels, only upward-preferring DSGCs exhibit broader direction tuning

- Broader tuning is produced by gap junctions and less-effective GABA inhibition

- This adaptation balances motion detection against direction discrimination

Authors

Xiaoyang Yao, Jon Cafaro,
Amanda J. McLaughlin,
Friso R. Postma, David L. Paul,
Gautam Awatramani, Greg D. Field

Correspondence

field@neuro.duke.edu

In Brief

Yao et al. demonstrate a novel form of light adaptation in ON-OFF DSGCs mediated by gap junctions and changes in effective GABA inhibition. Broader tuning at the low signal-to-noise ratio encountered at nighttime balances detection and direction estimation of motion.

Gap Junctions Contribute to Differential Light Adaptation across Direction-Selective Retinal Ganglion Cells

Xiaoyang Yao,[1,2] Jon Cafaro,[2] Amanda J. McLaughlin,[3] Friso R. Postma,[4] David L. Paul,[5] Gautam Awatramani,[3] and Greg D. Field[2,6,*]
[1]Graduate Program in Neurobiology, Duke University, Durham, NC, 27710, USA
[2]Neurobiology Department, Duke University School of Medicine, Durham, NC, 27710, USA
[3]Department of Biology, University of Victoria, Victoria, BC V8W 3N5, Canada
[4]Early Signal Foundation, New York, NY, USA
[5]Department of Neurobiology, Harvard Medical School, Boston, MA, 02115, USA
[6]Lead contact
*Correspondence: field@neuro.duke.edu
https://doi.org/10.1016/j.neuron.2018.08.021

SUMMARY

Direction-selective ganglion cells (DSGCs) deliver signals from the retina to multiple brain areas to indicate the presence and direction of motion. Delivering reliable signals in response to motion is critical across light levels. Here we determine how populations of DSGCs adapt to changes in light level, from moonlight to daylight. Using large-scale measurements of neural activity, we demonstrate that the population of DSGCs switches encoding strategies across light levels. Specifically, the direction tuning of superior (upward)-preferring ON-OFF DSGCs becomes broader at low light levels, whereas other DSGCs exhibit stable tuning. Using a conditional knockout of gap junctions, we show that this differential adaptation among superior-preferring ON-OFF DSGCs is caused by connexin36-mediated electrical coupling and differences in effective GABAergic inhibition. Furthermore, this adaptation strategy is beneficial for balancing motion detection and direction estimation at the lower signal-to-noise ratio encountered at night. These results provide insights into how light adaptation impacts motion encoding in the retina.

INTRODUCTION

Parallel processing and light adaptation are two salient aspects of retinal function. The encoding of visual scenes is partitioned across 30-40 distinct types of retinal ganglion cells (RGCs); each type tiles space with its receptive fields (RFs) and responds to distinct visual features (Baden et al., 2016; Sumbul et al., 2014). Concurrent with parallel processing, the retina must maintain sensitivity while avoiding saturation across the ten-billion-fold change in light intensity that separates a moonless night from a sunny day. This adaptation cannot be summarized by a simple gain change because the spatiotemporal structure of RGC RFs depends on light level. For example, center-surround antagonism (Kuffler, 1953), temporal integration (Field et al., 2009), response polarity (Pearson and Kerschensteiner, 2015; Tikidji-Hamburyan et al., 2015), and the linearity of spatial pooling (Grimes et al., 2014) all change between rod- and cone-mediated vision. Furthermore, adaptation appears to be RGC-type specific (Tikidji-Hamburyan et al., 2015), and thus it might alter how visual features produce responses across parallel pathways. The fact that the visual features encoded by RGCs depend on light level yokes light adaptation with parallel processing; this makes a complete understanding of one dependent on understanding the other.

One instance of this potential dependence is illustrated by direction-selective RGCs (DSGCs), which exhibit strong firing when visual stimuli move in a particular "preferred" direction but weak firing to the opposite "null" direction (Taylor and Vaney, 2002). DSGCs come in several types, including four types of ON-OFF DSGCs and at least three types of ON DSGCs (Elstrott et al., 2008; Hoshi et al., 2011; Kanjhan and Sivyer, 2010; Kim et al., 2008; Oyster and Barlow, 1967; Rivlin-Etzion et al., 2011; Rousso et al., 2016; Sabbah et al., 2017). These functionally distinct types are also distinguished by molecular markers (Dhande et al., 2013; Kay et al., 2011), exhibit distinct projections to the brain (Dhande and Huberman, 2014; Gauvain and Murphy, 2015; Huberman et al., 2009), and might mediate distinct behaviors (Sun et al., 2015). Furthermore, although ON-OFF DSGCs are frequently viewed as a single population, it is clear that they exhibit functional differences beyond their preferred directions. For example, superior-preferring ON-OFF DSGCs are electrically coupled by gap junctions, whereas cells preferring the other three directions are not coupled (Trenholm et al., 2013; Vaney, 1994). Gap junctions have been implicated as playing an important role in light adaptation (Bloomfield and Volgyi, 2004; Jin and Ribelayga, 2016), raising the possibility that superior-preferring ON-OFF DSGCs might adapt to light
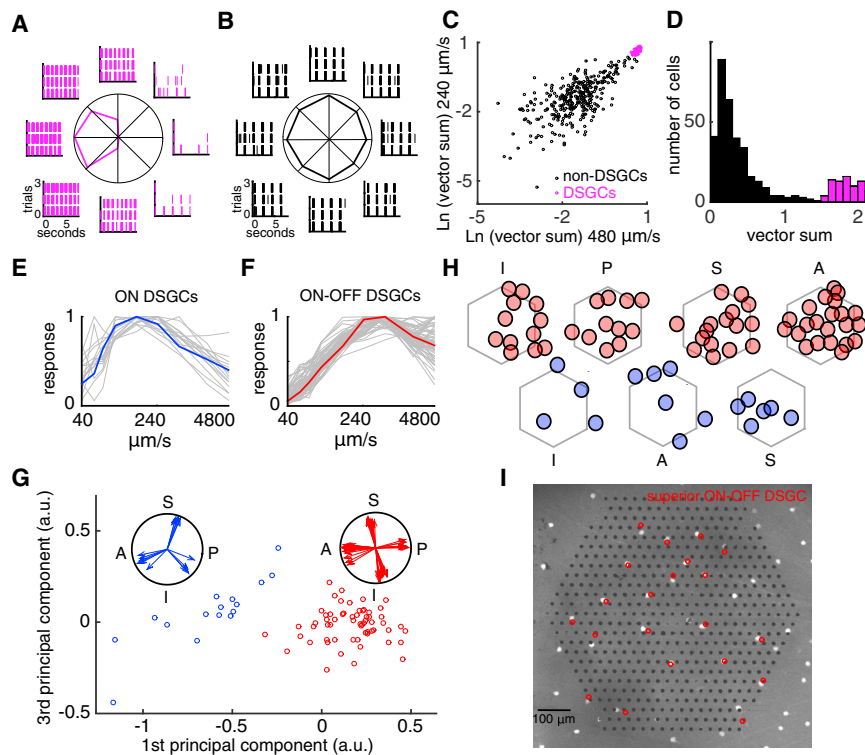
Figure 1. Functional Classification of DSGCs from Multielectrode Array Recordings

(A and B) Spike rasters of an example DSGC (A) and a non-DSGC (B) to square-wave gratings moving in eight directions at a speed of 480 μm/s (spatial period, 960 μm; temporal period, 2 s), 50% Michelson contrast, and background light intensity of 10,000 R*/rod/s. Each grating was represented pseudo-randomly three times. Polar plots summarize the average response in each direction normalized by the direction producing the highest firing rate.

(C) Vector sum magnitudes for drifting gratings presented at two different speeds (480 μm/s and 240 μm/s) from all RGCs identified in one MEA recording. Cells were clustered into DSGCs (magenta, n = 77 cells from one retina) and non-DSGCs (black, n = 328 cells from one retina) (see STAR Methods).

(D) Histogram of vector magnitudes for RGCs in (C)) in response to the 240 μm/s gratings.

(E and F) Speed tuning curves of ON DSGCs (E) and ON-OFF DSGCs (F); gray shows all cells of each type, and blue and red curves highlight an example ON and ON-OFF DSGC, respectively. Normalized response is computed on the basis of vector sum magnitudes (see STAR Methods).

(G) The scatterplot shows the weights from principal-component analysis of the speed tuning curves of all DSGCs in one recording: weights for first and third principal components are plotted. Cells were clustered into ON DSGCs (blue, n = 16 cells from one retina) and ON-OFF DSGCs (red, n = 61 cells from one retina) with a two-Gaussian mixture model. Polar plots indicate ON DSGCs (blue) aligned with three cardinal axes (left, blue) and ON-OFF DSGCs aligned with four cardinal axes (right, red). Note: coordinates are in visual space such that "superior" refers to upward motion in the environment (ventral on the retina). Abbreviations are as follows: S, superior; A, anterior; I, inferior; and P, posterior.

(H) ON (blue) and ON-OFF (red) DSGC locations for each preferred direction estimated from electrical images (see STAR Methods). Grey hexagons indicate the MEA border. Each circle has a diameter of 150 μm in approximation of the average dendritic field size of mouse DSGCs.

(I) Micrograph of whole-mount Hb9::eGFP retina on MEA. Bright dots are eGFP-expressing cells, which are ON-OFF superior-preferring DSGCs. Black dots are electrodes. Red circles indicate soma locations of ON-OFF superior-preferring DSGCs as estimated from electrical images (EIs, see STAR Methods and Figure S1).

differently from other DSGC types. Determining the extent to which light adaptation is heterogeneous across DSGCs is necessary for understanding how the retina encodes motion across day and night.

Here we use large-scale multi-electrode array (MEA) recordings from mouse retina to examine how the direction tuning of multiple subtypes of DSGCs depends on light level. We find that among ON-OFF DSGCs, superior-preferring cells broadened their direction tuning at low light levels, whereas this broadening was not present in other DSGC types. We show that this functional asymmetry in light adaptation is largely caused by two mechanisms: gap-junction-mediated electrical coupling and a reduction in effectual GABA-mediated inhibition. We further show that this asymmetry in direction tuning at low light levels strikes a balance between improving the detection of motion in dimly lit conditions against a cost to the accuracy of direction estimation. These results reveal how motion-sensitive neurons adapt to changes in the ambient light level and highlight how adaptation can tune parallel processing in neural populations to meet challenges imposed by changes in signal and noise.

RESULTS

Functionally Classifying Direction-Selective Ganglion Cells from Population Recordings

To measure changes in DSGC function across light levels from extracellular MEA recordings, one must reliably distinguish DSGCs from other simultaneously recorded cells and functionally classify them into distinct ON and ON-OFF subtypes (Elstrott et al., 2008; Fiscella et al., 2015; Sabbah et al., 2017). To identify the DSGCs, we presented square wave gratings moving in different directions while recording spike responses from the ganglion-cell layer of dorsal retina (Elstrott et al., 2008). When moving in the "preferred" direction, the gratings elicited strong responses in DSGCs, whereas they elicited weak responses when movement was in the "null" direction (Figure 1A). In contrast, responses of non-DSGCs were not dependent on motion direction (Figure 1B). We distinguished DSGCs from other RGCs by fitting a two-Gaussian mixture model to the vector sum of responses to gratings moving at two speeds under photopic conditions (Figure 1C, see STAR Methods). One Gaussian model captured DSGCs (Figure 1C and 1D, magenta), while

the second Gaussian model captured all other RGCs. This procedure avoided drawing an arbitrary threshold to distinguish these populations.

To distinguish ON from ON-OFF DSGCs, we leveraged their distinct speed tuning: ON DSGCs preferred relatively slow speeds (Figure 1E), whereas ON-OFF DSGCs responded to a broader range of speeds (Figure 1F) (Oyster, 1968; Sivyer et al., 2010; Wyatt and Daw, 1975). The speed tuning curves were analyzed by principal-component analysis (PCA), which allowed a low-dimensional representation of the differences in speed tuning between ON and ON-OFF DSGCs (Figure 1G; see STAR Methods). A two-Gaussian mixture model distinguished the two cell classes (Figure 1G, red versus blue). The group of cells preferring higher speeds exhibited an organization along four cardinal directions (Figure 1G, red), whereas the group of cells that preferred lower speeds exhibited an organization along three cardinal directions (Figure 1G, blue). This result is consistent with previous work examining the preferred directions of ON and ON-OFF DSGCs ([Oyster and Barlow, 1967; Vaney et al., 2012], but see [Baden et al., 2016; Sabbah et al., 2017]). Note that the coordinates for direction preferences are in visual space (e.g., "superior" corresponds to ventral motion on the retina and upward motion in the environment; see STAR Methods). Analyzing the spatial locations of the DSGCs from their electrical images (EIs; see STAR Methods) suggested that each population exhibited a mosaic-like organization (Figure 1H). Furthermore, an analysis of the distance to the nearest neighbor revealed an exclusion zone around each cell within a mosaic (Figure S1E). These results suggest that each group comprised an irreducible cell type (Devries and Baylor, 1997; Field et al., 2007; Vaney et al., 2012; Wassle et al., 1981).

To further validate the identification and classification of DSGCs, we used the HB9::GFP mouse line, which exhibits GFP expression in superior-preferring ON-OFF DSGCs (Trenholm et al., 2011). We tested for a spatial match between the GFP-positive cells and functionally identified superior-preferring ON-OFF DSGCs (Figure 1I and Figure S1) (Li et al., 2015). By comparing the locations of recorded RGCs to the location of GFP-positive cells (see STAR Methods), we found that functionally identified superior-preferring ON-OFF DSGCs exhibited a high degree of alignment with GFP-positive cells (Figure 1I), whereas other types of functionally identified DSGCs were located randomly with respect to GFP-positive cells (Figures S1C and S1D). These results validate the functional classification of DSGCs by matching a functionally defined type to a genetically defined type.

Direction Tuning of Superior-Preferring DSGCs Depends on Ambient Light Level

Having developed an approach to identify and record simultaneously from seven DSGC types, we next examined the extent to which the response properties of these cells depended on light level. We measured direction tuning curves of DSGCs by using drifting gratings at light levels ranging from 1 to 10,000 photoisomerizations (R*) per rod per second (8500 R*/M-cone/s); this spans rod and cone-mediated vision. We quantified the direction tuning of each type by calculating their direction selectivity indices (DSIs) and direction tuning widths (see STAR

Methods). Whereas anterior, inferior, and posterior ON-OFF DSGCs exhibited relatively stable tuning across light levels (Figures 2B–2D and 2F–2H) (ANOVA on the DSIs: anterior, p = 0.13; inferior, p = 0.57; posterior, p = 0.50) (ANOVA on the tuning width: anterior, p = 0.07; inferior, p = 0.21; posterior, p = 0.002), the direction tuning of superior-preferring ON-OFF DSGCs broadened as light levels decreased below cone threshold (Figures 2A and 2E) (p < 1.1×10^{-7}, ANOVA on DSI and tuning widths). We also found that the DSI of superior-preferring DSGCs was lower than those of the other three types under scotopic conditions (Figure 2I and Figure S2F; p < 0.001 for comparisons with each of the three other DSGC types). Their tuning widths were also broader than those of the other three types under scotopic conditions (Figure 2J, p < 0.001 for comparisons with each of the three other DSGC types). Note that spontaneous activity (Figure S2E) was subtracted, so responses to stimuli in the null direction represent a change in spike rate above baseline. All calculations of DSI and tuning width include this subtraction. These results reveal the impact of adaptation across the population of ON-OFF DSGCs: as light level decreases, DSGC population tuning switches from homogeneous (all narrow) to heterogeneous (three narrow, one wide; Figures 2J and 2K).

We also analyzed direction tuning of simultaneously recorded ON DSGCs (Figures S2A–S2D). These cells exhibited consistent and stable direction tuning across subtypes and light levels. Thus, we focus on ON-OFF DSGCs for the remaining analyses.

Conditional Knockout of *Cx36* Attenuates ON-OFF DSGC Coupling

What mechanisms cause superior-preferring ON-OFF DSGCs to light-adapt distinctly from other DSGC types? One likely mechanism is the Cx36-mediated homotypic gap-junction coupling that only these DSGCs exhibit (Trenholm et al., 2013; Vaney, 1994). This coupling could enable excitation to more effectively drive spikes in superior-preferring ON-OFF DSGCs (Trenholm et al., 2014). To test for a role of gap junctions in the broadening of DS tuning at low light levels, we developed a conditional knockout mouse in which gap-junction coupling is selectively disrupted among superior-preferring ON-OFF DSGCs. The mouse line contains a homozygous floxed *Cx36* allele (see STAR Methods and Figures S3I–S3K), a Fstl4-Cre allele for tamoxifen-dependent Cre expression in ON-OFF superior-preferring DSGCs (Kim et al., 2010), and a floxed tdTomato transgene to report functional Cre-mediated recombination (Figure 3A)(Madisen et al., 2010). Developing a conditional knockout mouse was critical because transmission of rod signals through both the primary and secondary rod pathways is dependent on Cx36 (Figure 3B)(Bloomfield and Dacheux, 2001). We refer to these animals as FACx mice.

To determine the extent to which coupling was reduced among superior-preferring ON-OFF DSGCs in FACx mice, we compared the spread of neurobiotin between tdTomato-positive RGCs in these mice and GFP-positive RGCs in Hb9::GFP mice. Hb9::GFP mice were used as the control group because they express GFP exclusively in superior-preferring ON-OFF DSGCs (and are thus easily targeted) but exhibit normal levels of
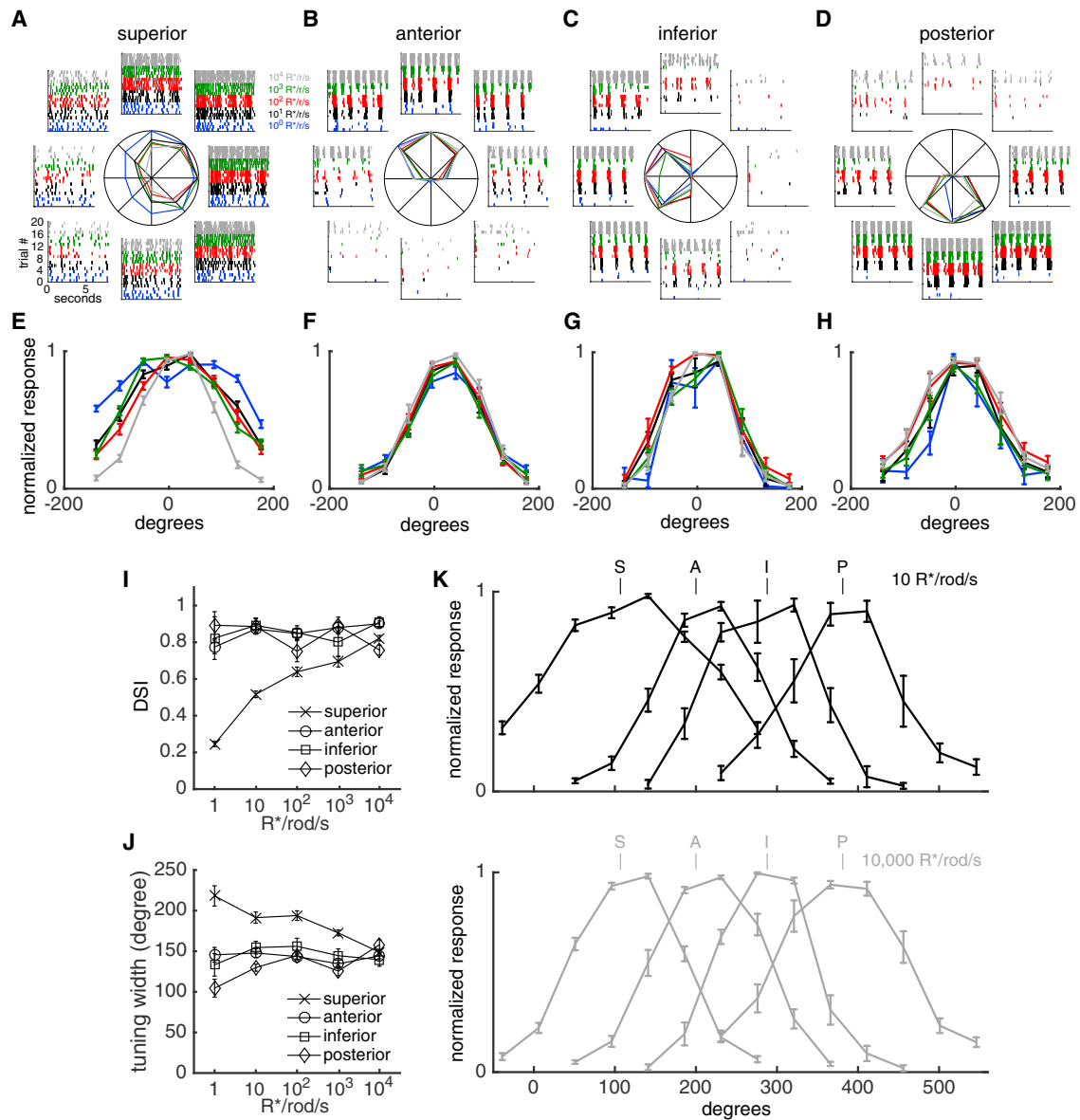
Figure 2. Direction Tuning of Superior-Preferring DSGCs Is Dependent on Ambient Light Level

(A–D) Response of example ON-OFF DSGCs to gratings moving in eight directions at a speed of 480 μm/s (spatial period, 960 μm; temporal period, 2 s) and 50% Michelson contrast across five light levels. Polar plots summarize direction tuning across light levels; data are normalized to the preferred direction response at each light level.

(E–H) Normalized average spike count as a function of stimulus direction across cells for each type in one retina. (mean ± SEM; data from one retina; superior, n = 18 cells; anterior, n = 22 cells; inferior, n = 7 cells; posterior, n = 11 cells). Note: we subtracted spontaneous (baseline) spiking from each cell prior to normalizing and averaging their tuning curves. See also Figure S2 for direction tuning curves of ON DSGCs.

(I) Direction selectivity index (see STAR Methods) as a function of background light intensity. Cells from two retinas were combined. (mean ± SEM; retina 1—same as [E–H]; retina 2—superior, n = 20 cells; anterior, n = 14 cells; inferior, n = 6 cells; and posterior, n = 6 cells)

(J) Tuning width (see STAR Methods) as a function of background light intensity. Cells from two retinas were combined (mean ± SEM; same as [I]).

(K) Average direction tuning curves for all four types of DSGCs at two different light levels (top, 10 R*/rod/s; bottom, 10,000 R*/rod/s; mean ± SEM; cells from one retina, same as [E–H]).

homotypic gap-junction coupling, as judged by neurobiotin diffusion (Figure 3C) (Trenholm et al., 2011). In FACx mice, neurobiotin diffusion indicated an attenuation in tracer coupling relative to that in Hb9::GFP animals (Figure 3C and Figures S3A–S3H). Note, even constitutive *Cx36* KO animals exhibited

some residual tracer coupling between superior-preferring ON-OFF DSGCs (Figure S3G), probably because these cells also express Cx45 (Schubert et al., 2005). Nevertheless, FACx animals exhibited reduced homotypic tracer coupling among superior-preferring ON-OFF DSGCs.
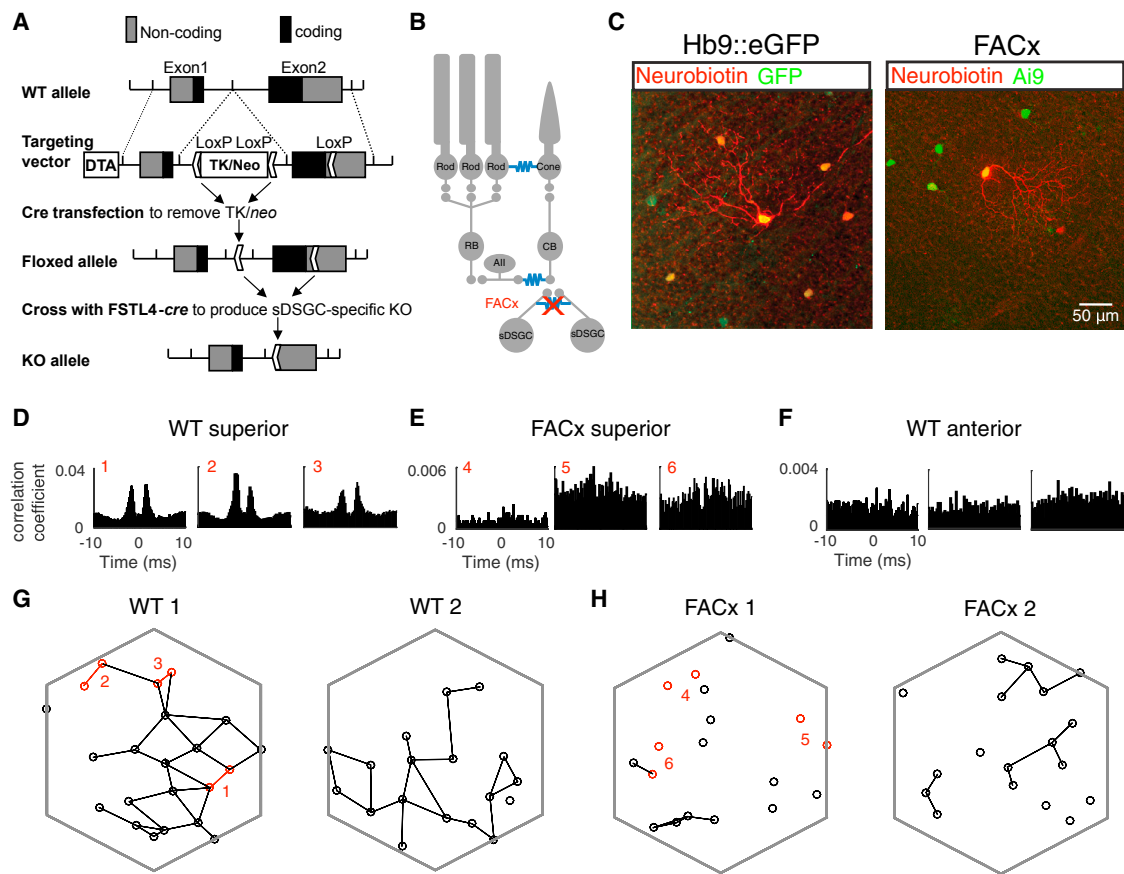
Figure 3. Electrical Coupling among Superior-Preferring ON-OFF DSGCs Is Reduced in FACx Mice

(A) Schematic depiction of the floxed Cx36 and FACx transgenic mouse lines.

(B) Circuit diagram showing the site of Cx36 knockout in FACx mice.

(C) Neurobiotin labeling of superior-preferring ON-OFF DSGCs. Left: Hb9::eGFP retina. Somata of superior-preferring ON-OFF DSGCs are eGFP$^+$ (green). Injection of the gap-junction-permeable tracer Neurobiotin into a single eGFP$^+$ cell revealed dye coupling to several neighboring somata (red). Right: FACx retina. Somata of CreER-expressing cells are tdTomato$^+$ (green). Injection of Neurobiotin into a single tdTomato$^+$ revealed some residual coupling with nearby cells (red). Injections were performed under mesopic conditions (50–500 Rh*/rod/s). See also Figure S3 for details.

(D–F) Example cross-correlograms computed for spike trains evoked by fine-scale checkerboard white noise (see STAR Methods) at 10,000 R*/rod/s for three example pairs of superior-preferring DSGCs in C57/bl6 (D), superior-preferring DSGCs in FACx (E), and anterior DSGCs in C57/bl6 (F). See also Figure S4 for change of correlated activity across light levels.

(G–H) Electrical coupling networks for two C57/bl6 (G) and two FACx retinas (H). Hexagons indicate outline of MEA. Each circle indicates estimated locations of superior-preferring ON-OFF DSGCs from their electrical images. Black lines connecting circles indicate electrically coupling cell pairs (see STAR Methods). Red circles and lines identify numbered example cell pairs in (D) and (E).

Functional electrical coupling between superior-preferring ON-OFF DSGCs was strongly attenuated in FACx mice. To assess electrical coupling, we analyzed the cross-correlation of spike trains between pairs of superior-preferring ON-OFF DSGCs. Direct electrical coupling manifests as temporally precise, bimodal peaks in the cross-correlation between two spike trains (Brivanlou et al., 1998; DeVries, 1999; Trenholm et al., 2014). In control mice (C57/bl6), cross-correlograms of spike trains from neighboring superior-preferring ON-OFF DSGCs exhibited sharp bimodal peaks in response to checkerboard noise (Figure 3D). This structure indicates that when one cell generates an action potential, the neighboring cell is significantly more likely to generate a spike ~2 ms later. These bimodal peaks were detected between most neighboring pairs of superior-

preferring ON-OFF DSGCs in C57/bl6 mice (Figure 3G; 35 of 49 neighbors; see STAR Methods). Bimodal peaks were almost entirely absent from the cross-correlograms of ON-OFF DSGCs that preferred other directions (Figure 3F; only 1 of 95 neighboring pairs met the threshold for a bimodal peak). These results show that ON-OFF superior-preferring DSGCs form a strongly coupled network in control retinas.

In FACx animals, electrical coupling between neighboring ON-OFF superior-preferring DSGCs was strongly attenuated (Figure 3E). Across the population, many fewer neighboring cell pairs exhibited bimodal peaks (Figure 3H). Control analyses indicated that this change in coupling could not be explained by differences in the number of spikes observed in superior-preferring ON-OFF DSGCs between WT and FACx mice (see STAR

A

B
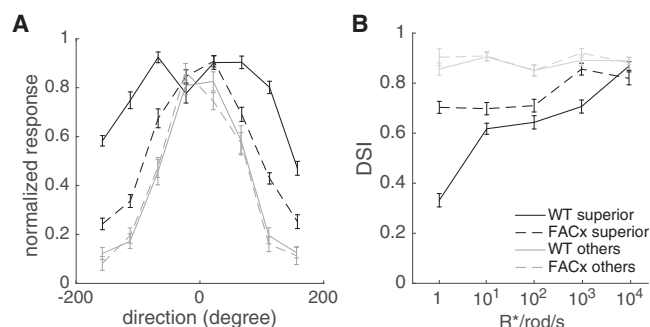
Figure 4. Direction Tuning of Superior-Preferring DSGCs at Low Light Levels Is Sharpened in FACx Mice

(A) Average direction tuning curves at 1 R*/rod/s of superior-preferring DSGCs in C57/bl6 mice (solid black line, n = 18 cells from one retina), FACx mice (dash black line, n = 37 cells from two retinas), and the other three types of DSGCs in C57/bl6 (solid gray line, n = 28 cells from one retina) and FACx (dashed gray line, n = 47 cells from two retinas). Note: we subtracted spontaneous (baseline) spiking from responses prior to normalizing and averaging the tuning curves. Data are represented as means ± SEM.

(B) Average DSI of superior-preferring and other DSGCs in WT (two retinas; superior, n = 38 cells; others, n = 63 cells) and FACx (two retinas; superior, n = 37 cells; others, n = 47 cells) mice as a function of background light level. Data are represent means ± SEM. See also Figure S5 for details.

Methods). We interpret the residual coupling in some pairs of FACx mice as cells in which tamoxifen administration failed to drive Cre-mediated recombination and excision of the floxed *Cx36* gene (Figure 3H; 15 of 36 neighbors). Thus, these experiments indicate that strong reciprocal electrical coupling that synchronizes spiking across the population of superior-preferring DSGCs is dependent upon *Cx36* expression and that the frequency of this coupling is appreciably reduced in FACx animals.

Light-Level-Dependent Changes in Tuning Partly Rely on Electrical Coupling

We next tested the impact of attenuated electrical coupling between superior-preferring ON-OFF DSGCs on their direction tuning. At low light levels (1 R*/rod/s), direction tuning of superior-preferring ON-OFF DSGCs was substantially narrower in FACx mice than in wild-type mice (p < 0.001), but it was still broader than that of DSGCs preferring other directions (Figure 4A and 4B, p < 0.001). In fact, DSIs did not converge until the brightest tested light levels (Figure 4B). This change in tuning width was restricted to the superior-preferring ON-OFF DSGCs; cells preferring other directions exhibited normal tuning widths across light levels in FACx mice (Figures 4A and 4B).

To test the possibility that residual coupling among some superior-preferring ON-OFF DSGCs produced a partial narrowing of tuning curves at low light levels, we compared tuning widths among superior-preferring ON-OFF DSGCs from putative knockout cells to those from putative normal cells (those that continued to express *Cx36*) in FACx mice (see STAR Methods). No significant difference in DSI was observed between these two populations (Figure S5A, p = 0.26), indicating that the incomplete narrowing was not caused by incomplete knockout of *Cx36*. This is most likely due to the fact that in cells that continue

to express *Cx36*, many homotypic neighbors do not express *Cx36*, and thus network coupling is still strongly attenuated. This interpretation is consistent with the fact that superior-preferring ON-OFF DSGCs in FACx mice exhibited a unimodal DSI distribution that was intermediate between WT superior-preferring cells and cells preferring one of the other three directions (Figure S5B). These results indicate that the broader direction tuning of superior-preferring DSGCs at low light levels is partly attributable to their gap-junction coupling.

We also tested the extent to which the strength of electrical coupling depended on light level. If electrical coupling was substantially stronger at lower light levels, this could explain the light-level-dependent change in direction tuning. We analyzed the amplitudes of the bimodal peaks in the cross-correlated spike trains across light levels. This indicated that coupling strength weakly depended on light level and revealed a small decrease in apparent coupling at high light levels (Figure S4).

The two observations of (1) a weak relationship between coupling strength and light level (Figure S4) and (2) residual broad tuning after the excision of *Cx36* (Figure 4) suggest that an additional mechanism is involved in broadening superior-preferring DSGC tuning at low light levels.

At Low Light Levels, Superior-Preferring ON-OFF DSGCs Receive Less Effective GABAergic Inhibition Than Other Types of DSGCs

Analyzing superior-preferring ON-OFF DSGC responses to bars moving in the null direction provided a clue to the additional mechanism. Similar to gratings, moving bars produced broader tuning among superior-preferring ON-OFF DSGCs than among other DSGC types at low light levels and a smaller difference between preferred- and null-direction stimuli (Figures S5C, S5G, and S5H). However, bars provided better separation between evoked and spontaneous firing on individual trials than did gratings, thus allowing for a more accurate estimate of responses to null-direction motion. Under scotopic conditions, superior-preferring ON-OFF DSGCs exhibited clear responses to null-direction bars: other ON-OFF DSGCs exhibited minimal responses (Figure 5A, left). The differences in the null-direction responses were present across a range of bar contrasts (Figure 5B). This observation suggests that at low light levels, inhibition might less effectively attenuate null-direction responses in superior-preferring ON-OFF DSGCs than in other DSGC types. The difference might also reflect other factors, such as greater excitation in superior-preferring ON-OFF DSGCs.

To test this idea further, we used the GABA_A receptor antagonist gabazine (SR-95531) to attenuate the major inhibitory input onto DSGCs (Pei et al., 2015; Yoshida et al., 2001). If superior-preferring DSGCs receive less-effective GABA_A-mediated inhibition than other DSGC types but similar excitation, then gabazine should effectively equate their contrast response functions to bars moving in the null direction. As expected, application of gabazine increased null-direction responses for both superior-preferring and other DSGCs (Figure 5A, right). However, across bar contrasts, the increase in spike rate with gabazine was much less for superior-preferring DSGCs than the other types (Figure 5B): e.g., at 80% bar contrast, superior-preferring
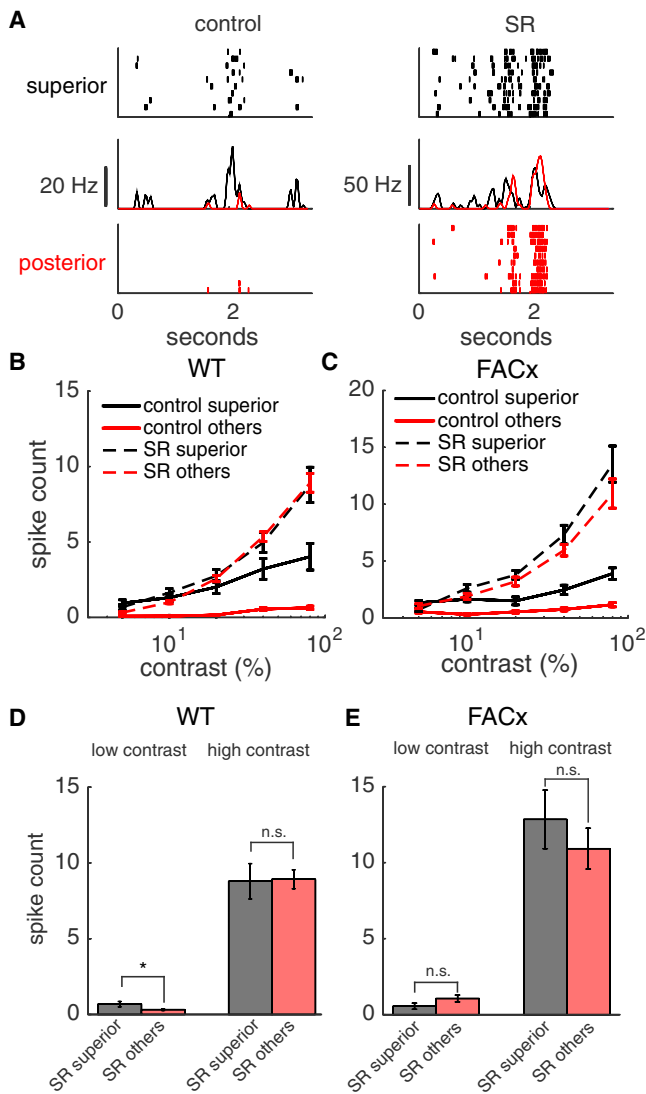
Figure 5. Gabazine Equates the Null-Direction Responses among All Types of ON-OFF DSGCs at Low Light Levels

(A) Top: spike rasters of a superior-preferring DSGC in control (left) and 15 μM SR (right) conditions in response to 10 repeats of a bar (80% positive contrast) moving in the null direction at a speed of 960 μm/s with a background light intensity of 4 R*/rod/s. Bottom: spike rasters of a posterior DSGC. Middle: overlaying PSTHs of the superior- and posterior-preferring DSGCs in control and SR conditions.

(B and C) Average number of spikes, as a function of bar contrast, in a 1 s time bin in response to a bar moving in the null direction in C57 ([B] two retinas; superior, n = 20 cells; others, n = 50 cells) and FACx ([C] two retinas; superior, n = 11 cells; others, n = 23 cells). Data are represent means ± SEM.

(D and E) Summary of spike counts of superior-preferring and other DSGCs in control and SR conditions at low (5%) and high (80%) contrasts in C57 (D) and FACx (E) (same population of cells as in [B] and [C]). Data are represent means ± SEM. See also Figure S5 for a LIF model simulation.

versus other DSGCs exhibited 2- versus 12-fold increases, respectively. Most importantly, their responses were nearly equal across contrasts in the presence of gabazine. This near equating of the responses of superior-preferring and other

DSGCs by gabazine at low light levels did not depend on the direction of motion (Figures S5E and S5F), lending further support to the idea that the major difference could be localized to differences in the effective GABA_A-mediated inhibition.

The small residual difference in null-direction responses between superior-preferring and other DSGCs under gabazine was primarily present for low-contrast bars (Figure 5B). At high bar contrasts (40%–100%), there was no significant difference between null-direction responses (Figure 5B and 5D, $p > 0.1$). However, at low contrasts (5%–10%), the null-direction responses were significantly larger for superior-preferring DSGCs than for the other types, even in the presence of gabazine (Figure 5B and 5D, $p < 0.05$). This difference of null-direction responses at low contrasts disappeared when the same experiment was performed in FACx mice (Figure 5C and 5E, $p > 0.1$), suggesting that the difference at low contrasts in wild-type mice was attributable to electrical coupling.

The equating of null-direction responses between superior-preferring and other DSGCs in the presence of gabazine in FACx mice (Figure 5E) is consistent with the idea that these two mechanisms can account for the differences in null-direction spiking at low light levels. To test the plausibility that these two mechanisms work together to broaden the tuning of superior-preferring DSGCs at low light levels, we generated a simple biophysical model of a network of superior-preferring DSGCs (Figures S5I–S5K; see STAR Methods). Under conditions of strong inhibition, the presence of gap junctions had minimal impact on the tuning width (Figure S5L). However, when inhibition was decreased, network coupling further broadened DSGC tuning (Figure S5M). Thus, we suggest that decreased GABAergic suppression of responses to stimuli moving in the null direction results in greater net excitation impinging on superior-preferring DSGCs, and this greater excitation is accentuated by homotypic electrical coupling (Trenholm et al., 2014) (See Discussion).

Broad Tuning Balances Motion Detection against Direction Discrimination

What is the benefit of switching from homogeneous tuning widths by all DSGCs under photopic conditions to broader tuning and increased null-direction responses for one type of DSGC under scotopic conditions? In general, broader tuning can be beneficial for detecting stimuli but can come at the cost of discriminating small changes in the encoded feature (Butts and Goldman, 2006; Fiscella et al., 2015; Seung and Sompolinsky, 1993). Thus, we hypothesized that the population of all ON-OFF DSGCs might strike a balance between detecting motion and accurately signaling direction at low light levels. This balance might be different under rod- versus cone-mediated visual conditions because in general, the signal-to-noise ratio (SNR) is lower under scotopic conditions (Barlow and Levick, 1969).

We first tested whether DSGCs exhibit a change in their response SNR (mean/SD of responses in preferred direction) between high and low light levels. Using moving bars to probe the responses of DSGCs, we found that the response SNR under scotopic conditions was less than half that under photopic conditions for most cells (Figure 6B, $p < 0.001$, see STAR Methods).
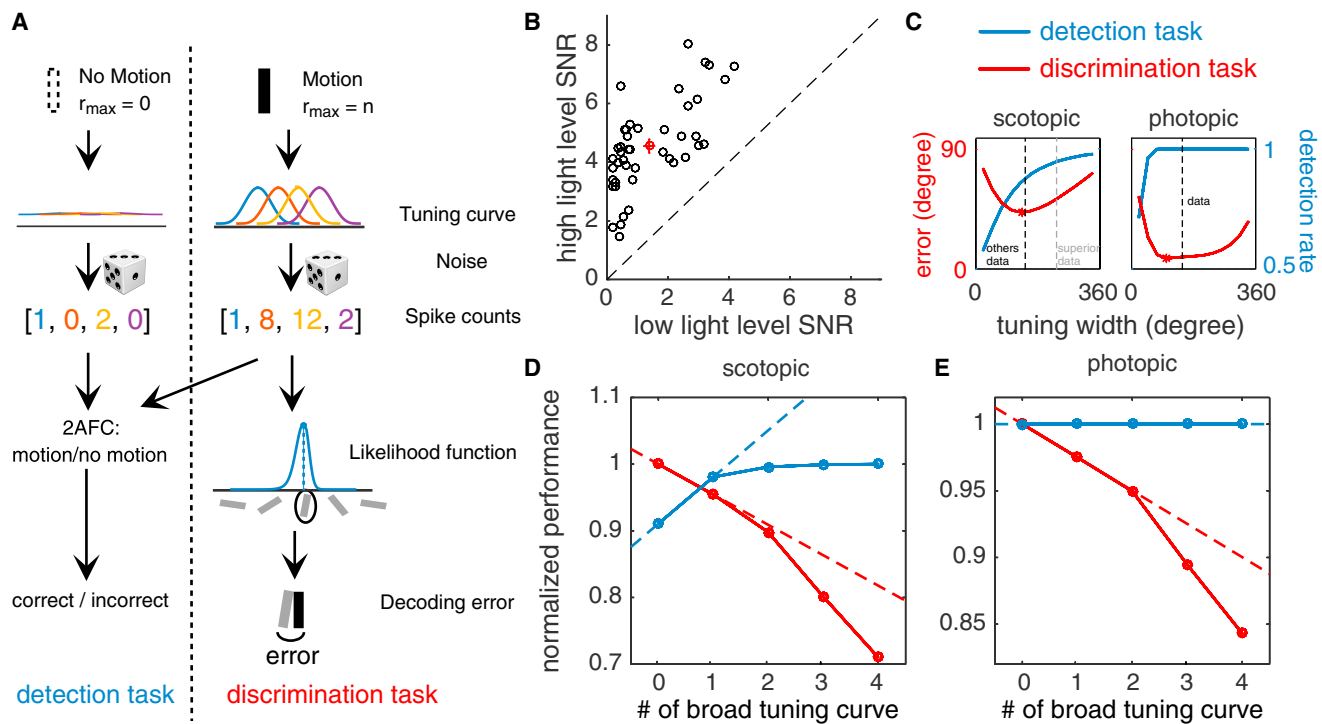
Figure 6. Impact of Direction Tuning Width on Motion Detection and Discrimination

(A) Schematic depiction of simulated motion-detection (left) and direction-discrimination (right) tasks (see STAR Methods).

(B) Black circles indicate SNR of an individual DSGC (all direction preferences) at 20% bar contrast at two different light levels (low light level—1 R*/rod/s; high light level—10,000 R*/rod/s). A red circle indicates the average SNR across cells. (means ± SEM; 1 retina, n = 64 cells). Data from another retina have the same result (not shown).

(C) Simulated discrimination error (red) and detection rate (blue) as a function of direction tuning width [α in Equation 2, β fixed to 1] at rod (1 R*/rod/s, R_{max} = 1.5) and cone (10,000 R*/rod/s, R_{max} = 7.7) light levels. Red stars mark the lowest points on the discrimination error curves. Dashed lines mark the tuning widths measured from MEA recordings with drifting gratings.

(D and E) Normalized performance changes (see STAR Methods) in discrimination (red) and detection (blue) tasks as a function of the number of broad tuning curves in the DSGC population at rod (D) and cone (E) light levels (1 R*/rod/s and 10,000 R*/rod/s, respectively). See also Figure S6 for detection and discrimination as a function of stimulus direction.

Using these SNR measurements, we next simulated DSGC spiking responses to moving bars to estimate the performance of quartets of orthogonally tuned ON-OFF DSGCs in two tasks: motion detection and discrimination of motion direction (Figure 6A, see STAR Methods). We analyzed the relationship between the SNR of DSGC responses and optimal tuning width by varying the tuning width (α in Equation 2) under low- (rod) and high- (cone) SNR conditions. Note that in these simulations the tuning curve width of all four DSGCs changed together. The purpose of this analysis is to reveal how a change in DSGC SNR impacts optimal tuning widths in these tasks while other parameters of DSGC tuning are held constant. At the photopic SNR, detection performance rose monotonically with tuning curve width and rapidly approached an asymptote of one, whereas the direction discrimination error exhibited a U-shaped function with a minimum near 100 degrees (Figure 6C, right). DSGC tuning widths were near this optimal value (Figure 6C, right, vertical line) but were slightly broader, as reported previously (Fiscella et al., 2015). At scotopic SNRs, detection performance rose less rapidly, requiring broader tuning widths so as to reach a high detection rate (Figure 6C, left). Also, direction discrimination

error reached a minimum at broader tuning widths than under photopic SNRs. Thus, the lower SNR exhibited under scotopic conditions promotes broader direction tuning among a quartet of orthogonally tuned DSGCs.

Given the benefit of broader tuning curves at a low SNR as indicated by the previous analysis, why do three ON-OFF DSGC types retain narrow tuning under scotopic conditions? To answer this question, we tested for a trade-off between reliably detecting motion and accurately estimating direction. Such a trade-off is suggested at the rod SNR condition because the tuning width of the superior-preferring DSGCs produces better detection performance but produces greater errors in direction discrimination (Figure 6C left, vertical lines). Thus, in simulation, we tested the impact of making different numbers of DSGCs match the tuning of superior-preferring DSGCs under scotopic conditions (note: α, β, and R_{max} of Equation 2 all changed; see STAR Methods, *Decoding model*, and Figure S6).

This analysis revealed that under scotopic conditions, making one tuning curve broad had the largest proportional increase in detection performance; performance increased sublinearly with the number of broad tuning curves (Figure 6D, blue solid

versus blue dashed line). This indicates diminishing returns for motion detection when tuning of additional DSGC types broadens. Meanwhile, one broad tuning curve yielded the smallest relative cost in discrimination performance; performance decreased supra-linearly with the number of broad tuning curves (Figure 6D, red solid versus red dashed line). This indicates slightly accelerating costs for making additional directions exhibit broad tuning. Furthermore, this analysis indicated a balance in the relative cost-benefit between detection and discrimination at one cell type with broad tuning (red and blue curves cross near 1 broad tuning curve: Figure 6D). Under photopic conditions, making tuning curves broad produced no improvement in detection performance (Figure 6E). This is related to the rapidly saturating performance as a function of tuning width at high SNR (Figure 6C, right); there is minimal benefit to making tuning curves broader for detection under photopic conditions. However, there is a clear cost for direction-discrimination performance when the number of directions with broad tuning curves increases (Figure 6E). Thus, a balance between detection versus discrimination performance appears to be reached for all narrow tuning curves at high light levels and for one broad tuning curve at low light levels.

DISCUSSION

We simultaneously tracked the direction tuning of seven DSGC types across light levels and identified one type that exhibits a pronounced broadening of direction tuning and a smaller difference between responses to preferred and null directions under scotopic conditions. This broadening could be accounted for by two mechanisms: (1) Cx36-mediated homotypic gap-junction coupling and (2) less-effective GABAergic suppression of null-direction responses relative to other DSGCs. Via a model that incorporated SNR changes across light levels, we show that the observed adaptation strikes a balance between detecting motion and accurately signaling its direction.

Functional Classification of DSGCs

Many sensory features, such as color in the primate retina (Dacey, 2000), are encoded across neural populations composed of multiple cell types. Similarly, motion direction is encoded in the retina across an ensemble of DSGCs with cardinally organized direction preferences (Oyster, 1968; Sabbah et al., 2017). Understanding how such population codes adapt requires recording from many neurons, identifying cell types, and tracking these types across a broad range of conditions. From large-scale multielectrode array recordings, we developed a quantitative classification approach involving several serial steps: (1) distinguishing DSGCs from other RGCs; (2) distinguishing ON from ON-OFF DSGCs; and (3) subtyping on the basis of direction preference. We validated this classification in two ways. First, each subtype exhibited a mosaic-like spatial arrangement, a hallmark of cell types in the retina (Figure 1H) (Devries and Baylor, 1997; Yu et al., 2017). Second, we matched the spatial locations the superior-preferring ON-OFF DSGCs to GFP-positive neurons in the HB9::GFP line, which expresses GFP exclusively in these cells (Figure S1) (Hoggarth et al., 2015). This approach allowed measuring adaptation in a population code.

Early studies of DSGCs uncovered seven basic types: ON-OFF DSGCs aligned along four cardinal axes and ON DSGCs aligned along three cardinal axes (Oyster, 1968). Until recently, this was considered a complete accounting of DSGCs. Studies utilizing transgenic lines and population calcium imaging have suggested an OFF DSGC type ([Kim et al., 2008], but see [Nath and Schwartz, 2017]), a fourth type of ON DSGC (Sabbah et al., 2017), and potentially greater diversity within DSGCs that prefer a given direction (Baden et al., 2016; Rivlin-Etzion et al., 2011). Furthermore, studies in rabbits have indicated two varieties of ON DSGCs: sustained and transient cells (Hoshi et al., 2011; Kanjhan and Sivyer, 2010). We did not find evidence of these additional types. However, extracellular recordings and spike sorting are subject to biases that might prevent measuring signals from these cells. Thus, testing for these types and determining how they adapt to changes in ambient light level will require further studies.

We have focused our analysis on the detection and discrimination of motion from ON-OFF DSGCs because several lines of evidence suggest the ON DSGCs constitute a distinct system. First, ON DSGCs more sparsely sample visual scenes with larger spatial RFs. Second, they are tuned for lower speeds. Third, ON and ON-OFF DSGCs exhibit different projection patterns to different brain areas. ON DSGCs primarily project to the accessory optic system (Dhande et al., 2013; Simpson, 1984), whereas ON-OFF DSGCs project robustly to the dLGN and the superior colliculus (Kay et al., 2011). Although some overlap in their project patterns has been observed (Gauvain and Murphy, 2015; Kay et al., 2011), it is not clear that any brain area receives direct projections from all ON and ON-OFF DSGCs.

Mechanisms for Broader Tuning of Superior-Preferring ON-OFF DSGCs

We found that at least two mechanisms probably contribute to the broader tuning of superior-preferring ON-OFF DSGCs at low light levels. The first one is homotypic gap-junction coupling among these cells. Gap junctions are present in all five major neuron classes in the vertebrate retina (Bloomfield and Volgyi, 2009; Sohl et al., 2005). Previous work has highlighted their contribution to light adaptation. In particular, modulation of gap-junction coupling throughout the retina might tune signal pooling to light-level-dependent changes in signal and noise (Baldridge et al., 1995; Hu and Bloomfield, 2003; Jin and Ribelayga, 2016; Lasater, 1987; Xin and Bloomfield, 1999). This study demonstrates an additional way in which gap junctions can contribute to adaptation: they can contribute to broadening direction tuning, thereby improving motion detection at low light levels. However, we have not directly addressed how gap junctions yield broader tuning in superior-preferring ON-OFF DSGCs at low, but not high, light levels. At least two processes could explain the light-dependent change. First, the strength of reciprocal coupling between DSGCs could increase at low light levels. Such modulation could be induced by the paracrine action of dopamine in the retina; retinal dopamine concentration rises with light level, and this has been shown to alter gap-junction coupling among other retinal cell types, such as horizontal cells (Hampson et al., 1994; Lasater, 1987; McMahon et al., 1989). We found evidence for a very modest increase in electrical coupling

between neighboring superior-preferring DSGCs at low light levels (Figure S4).

We also found evidence for a change in the effective GABAergic inhibition. Specifically, blocking GABA$_A$-mediated inhibition had a smaller effect on the null-direction responses of ON-OFF superior-preferring DSGCs than of other DSGCs at low light levels (Figure 5B). Importantly, blocking GABA$_A$-mediated inhibition also equated the null-direction responses of superior-preferring and other ON-OFF DSGCs across contrasts (Figure 5B) and across directions (Figures S5E–S5F). These observations suggest that superior-preferring ON-OFF DSGCS receive less-effective inhibition at low light levels than other ON-OFF DSGCs. In this hypothesized model, chemical excitatory inputs to the DSGC from stimuli at the flanks of the tuning curve would be less effectively canceled by inhibition either from pre- or post-synaptic sources. This excitation would be bolstered by the depolarization of nearby superior-preferring ON-OFF DSGCs in response to the moving bar, further broadening tuning. We tested this hypothesis in a simple biophysical model (Figures S5I–S5M), which qualitatively reproduced our data. Potentially, this effect could be amplified by a supra-linear combination of gap-junction input and chemical excitatory input to produce dendritic spikes. Just this sort of supra-linear interaction has been observed in superior-preferring ON-OFF DSGCs (Trenholm et al., 2014).

This hypothesis requires a cell-type- and light-level-specific change in either the amplitude or timing of inhibition impinging on superior-preferring ON-OFF DSGCs (or onto their inputs) in relation to excitation (Vaney et al., 2012). We have not identified the cellular and synaptic origin of this change. However, a recent study showed both light-level- and cell-type-specific changes in GABAergic inhibition in other RGC types (Pan et al., 2016). Furthermore, these differences in GABAergic inhibition have been shown to play a substantial role in setting the absolute threshold of RGC responses: cells receiving less inhibition respond to dimmer flashes of light (Pan et al., 2016). Additionally, several different types of amacrine cells have recently been observed to interact with DSGCs: VIP amacrine cells (Park et al., 2015), wide-field spiking amacrine cells (Hoggarth et al., 2015), and VGlut3 amacrine cells (Lee et al., 2014). At least the wide-field spiking amacrine cells exhibit a light-level dependent interaction with DSGC circuits (Hoggarth et al., 2015). Thus, a change in effective GABAergic inhibition in the superior-preferring ON-OFF DSGC circuit could be the dominant mechanism mediating the change in tuning. However, fully testing these models will require intracellular measurements that directly assay inhibition, excitation, and gap-junction-mediated conductance.

DSGC Motion Detection and Discrimination

Different portions of bell-shaped tuning functions are most reliable for detecting or discriminating stimuli (Butts and Goldman, 2006; Purushothaman and Bradley, 2005; Seung and Sompolinsky, 1993). For detection, neurons most reliably respond to stimuli aligned with the tuning-curve peak because these stimuli produce a response with the largest SNR. For discrimination, stimuli off-peak of the tuning curve—in the high-slope region—are most reliably distinguished because small changes in the

stimulus produce large changes in the response. A consequence of these principles is that broader tuning curves can detect a greater range of stimuli, whereas narrow tuning curves will have steeper slopes that provide better discrimination.

Previous work in the insect cercal system (Theunissen and Miller, 1991), which encodes the direction of wind, and the DSGC system in mammalian retina (Fiscella et al., 2015) has included analysis of optimal tuning widths for direction-selective neurons. These systems exhibit a high degree of similarity because each contains four canonical cell types with orthogonally organized direction preferences. In both systems, tuning widths across the population of neurons are near optimal for direction discrimination but are slightly broader than optimal, which minimally increases average error while reducing maximum errors (Fiscella et al., 2015; Salinas and Abbott, 1994). These studies estimated optimal tuning widths for direction discrimination at neural SNR values measured under a narrow range of stimulus conditions. Thus, previous work has not examined the extent to which the SNR of these neurons could change given different ambient light levels or wind conditions and how these may interact with stimulus detection.

We found that at low light levels, the SNR of DSGC responses was substantially lower (Figure 6B), primarily because of decreased firing rates. Lower SNR promotes broader tuning widths for optimal discrimination and detection (Figure 6C). However, because DSGC tuning widths are already broader than optimal (Fiscella et al., 2015), broadening all the tuning curves increases the average expected error in direction estimation. The case is different for motion detection, where lower SNR severely reduces the ability of the DSGC population to reliably signal the presence of motion. Thus, broader tuning curves improve detection performance under SNRs matched to those measured under scotopic conditions (Figure 6). Importantly, although broadening all tuning curves benefits detection performance, it diminishes discrimination performance. We found that broadening one of four tuning curves approximately balances the benefit to motion detection against the cost to direction discrimination. Our analysis of detection and discrimination indicates that idea is plausible, but a strong conclusion requires knowing how DSGC signals are processed by downstream circuits and how they are combined with the signals from other RGC types. Our analysis assumes that DSGCs are used for both motion detection and direction discrimination; other RGC types might contribute to these tasks as well. This points to an important direction for future work to understand how motion signals in the retina shape the activity of downstream circuits and behavior as well as how this activity depends on night versus daytime vision.

STAR★METHODS

Detailed methods are provided in the online version of this paper and include the following:

- KEY RESOURCES TABLE
- CONTACT FOR REAGENT AND RESOURCE SHARING
- EXPERIMENTAL MODEL AND SUBJECT DETAILS
  - Mice

SUPPLEMENTAL INFORMATION

Supplemental Information includes six figures and can be found with this article online at https://doi.org/10.1016/j.neuron.2018.08.021.

AUTHOR CONTRIBUTIONS

The project was conceived by X.Y. and G.D.F.. All physiology experiments and modeling were performed and analyzed by X.Y with assistance from J.C.. FACx mice were produced and validated by A.J.M and G.A., who also measured anatomical gap-junction-mediated coupling. Cx36-floxed mice were produced and validated by F.R.P and D.L.P.. The manuscript was written and edited by X.Y. and G.D.F.. All other authors provided comments during the editing stage.

DECLARATION OF INTERESTS

The authors declare no competing interests.

REFERENCES

Akimoto, M., Filippova, E., Gage, P.J., Zhu, X., Craft, C.M., and Swaroop, A. (2004). Transgenic mice expressing Cre-recombinase specifically in M- or S-cone photoreceptors. Invest. Ophthalmol. Vis. Sci. *45*, 42–47.

Applebury, M.L., Antoch, M.P., Baxter, L.C., Chun, L.L., Falk, J.D., Farhangfar, F., Kage, K., Krzystolik, M.G., Lyass, L.A., and Robbins, J.T. (2000). The murine cone photoreceptor: A single cone type expresses both S and M opsins with retinal spatial patterning. Neuron *27*, 513–523.

Baden, T., Berens, P., Franke, K., Roman Roson, M., Bethge, M., and Euler, T. (2016). The functional diversity of retinal ganglion cells in the mouse. Nature *529*, 345–350.

Baldridge, W.H., Weiler, R., and Dowling, J.E. (1995). Dark-suppression and light-sensitization of horizontal cell responses in the hybrid bass retina. Vis. Neurosci. *12*, 611–620.

Barlow, H.B., and Levick, W.R. (1969). Changes in the maintained discharge with adaptation level in the cat retina. J. Physiol. *202*, 699–718.

Bekkers, J.M., and Stevens, C.F. (1996). Cable properties of cultured hippocampal neurons determined from sucrose-evoked miniature EPSCs. J. Neurophysiol. *75*, 1250–1255.

Bloomfield, S.A., and Dacheux, R.F. (2001). Rod vision: Pathways and processing in the mammalian retina. Prog. Retin. Eye Res. *20*, 351–384.

Bloomfield, S.A., and Volgyi, B. (2004). Function and plasticity of homologous coupling between AII amacrine cells. Vision Res. *44*, 3297–3306.

Bloomfield, S.A., and Volgyi, B. (2009). The diverse functional roles and regulation of neuronal gap junctions in the retina. Nat. Rev. Neurosci. *10*, 495–506.

Brivanlou, I.H., Warland, D.K., and Meister, M. (1998). Mechanisms of concerted firing among retinal ganglion cells. Neuron *20*, 527–539.

Butts, D.A., and Goldman, M.S. (2006). Tuning curves, neuronal variability, and sensory coding. PLoS Biol. *4*, e92.

Carcieri, S.M., Jacobs, A.L., and Nirenberg, S. (2003). Classification of retinal ganglion cells: A statistical approach. J. Neurophysiol. *90*, 1704–1713.

Dabrowski, W., Grybos, P., and Litke, A.M. (2004). A low noise multichannel integrated circuit for recording neuronal signals using microelectrode arrays. Biosens. Bioelectron. *19*, 749–761.

Dacey, D.M. (2000). Parallel pathways for spectral coding in primate retina. Annu. Rev. Neurosci. *23*, 743–775.

Deans, M.R., and Paul, D.L. (2001). Mouse horizontal cells do not express connexin26 or connexin36. Cell Commun. Adhes. *8*, 361–366.

Deans, M.R., Volgyi, B., Goodenough, D.A., Bloomfield, S.A., and Paul, D.L. (2002). Connexin36 is essential for transmission of rod-mediated visual signals in the mammalian retina. Neuron *36*, 703–712.

DeVries, S.H. (1999). Correlated firing in rabbit retinal ganglion cells. J. Neurophysiol. *81*, 908–920.

Devries, S.H., and Baylor, D.A. (1997). Mosaic arrangement of ganglion cell receptive fields in rabbit retina. J. Neurophysiol. *78*, 2048–2060.

Dhande, O.S., Estevez, M.E., Quattrochi, L.E., El-Danaf, R.N., Nguyen, P.L., Berson, D.M., and Huberman, A.D. (2013). Genetic dissection of retinal inputs to brainstem nuclei controlling image stabilization. J. Neurosci. *33*, 17797–17813.

Dhande, O.S., and Huberman, A.D. (2014). Retinal ganglion cell maps in the brain: Implications for visual processing. Curr. Opin. Neurobiol. *24*, 133–142.

Eglen, S.J. (2006). Development of regular cellular spacing in the retina: theoretical models. Math. Med. Biol. *23*, 79–99.

Elstrott, J., Anishchenko, A., Greschner, M., Sher, A., Litke, A.M., Chichilnisky, E.J., and Feller, M.B. (2008). Direction selectivity in the retina is established independent of visual experience and cholinergic retinal waves. Neuron *58*, 499–506.

Feigenspan, A., Janssen-Bienhold, U., Hormuzdi, S., Monyer, H., Degen, J., Sohl, G., Willecke, K., Ammermuller, J., and Weiler, R. (2004). Expression of connexin36 in cone pedicles and OFF-cone bipolar cells of the mouse retina. J. Neurosci. *24*, 3325–3334.

Feigenspan, A., Teubner, B., Willecke, K., and Weiler, R. (2001). Expression of neuronal connexin36 in AII amacrine cells of the mammalian retina. J. Neurosci. *21*, 230–239.

Field, G.D., Gauthier, J.L., Sher, A., Greschner, M., Machado, T.A., Jepson, L.H., Shlens, J., Gunning, D.E., Mathieson, K., Dabrowski, W., et al. (2010). Functional connectivity in the retina at the resolution of photoreceptors. Nature *467*, 673–677.

Field, G.D., Greschner, M., Gauthier, J.L., Rangel, C., Shlens, J., Sher, A., Marshak, D.W., Litke, A.M., and Chichilnisky, E.J. (2009). High-sensitivity rod photoreceptor input to the blue-yellow color opponent pathway in macaque retina. Nat. Neurosci. *12*, 1159–1164.

Field, G.D., and Rieke, F. (2002). Nonlinear signal transfer from mouse rods to bipolar cells and implications for visual sensitivity. Neuron 34, 773–785.

Field, G.D., Sher, A., Gauthier, J.L., Greschner, M., Shlens, J., Litke, A.M., and Chichilnisky, E.J. (2007). Spatial properties and functional organization of small bistratified ganglion cells in primate retina. J. Neurosci. 27, 13261–13272.

Fiscella, M., Franke, F., Farrow, K., Muller, J., Roska, B., da Silveira, R.A., and Hierlemann, A. (2015). Visual coding with a population of direction-selective neurons. J. Neurophysiol. 114, 2485–2499.

Frechette, E.S., Sher, A., Grivich, M.I., Petrusca, D., Litke, A.M., and Chichilnisky, E.J. (2005). Fidelity of the ensemble code for visual motion in primate retina. J. Neurophysiol. 94, 119–135.

Gauvain, G., and Murphy, G.J. (2015). Projection-specific characteristics of retinal input to the brain. J. Neurosci. 35, 6575–6583.

Grimes, W.N., Schwartz, G.W., and Rieke, F. (2014). The synaptic and circuit mechanisms underlying a change in spatial encoding in the retina. Neuron 82, 460–473.

Hampson, E.C., Weiler, R., and Vaney, D.I. (1994). pH-gated dopaminergic modulation of horizontal cell gap junctions in mammalian retina. Proc. Biol. Sci. 255, 67–72.

Han, Y., and Massey, S.C. (2005). Electrical synapses in retinal ON cone bipolar cells: Subtype-specific expression of connexins. Proc. Natl. Acad. Sci. USA 102, 13313–13318.

Hoggarth, A., McLaughlin, A.J., Ronellenfitch, K., Trenholm, S., Vasandani, R., Sethuramanujam, S., Schwab, D., Briggman, K.L., and Awatramani, G.B. (2015). Specific wiring of distinct amacrine cells in the directionally selective retinal circuit permits independent coding of direction and size. Neuron 86, 276–291.

Hoshi, H., Tian, L.M., Massey, S.C., and Mills, S.L. (2011). Two distinct types of ON directionally selective ganglion cells in the rabbit retina. J. Comp. Neurol. 519, 2509–2521.

Hu, E.H., and Bloomfield, S.A. (2003). Gap junctional coupling underlies the short-latency spike synchrony of retinal alpha ganglion cells. J. Neurosci. 23, 6768–6777.

Huberman, A.D., Wei, W., Elstrott, J., Stafford, B.K., Feller, M.B., and Barres, B.A. (2009). Genetic identification of an On-Off direction-selective retinal ganglion cell subtype reveals a layer-specific subcortical map of posterior motion. Neuron 62, 327–334.

Jin, N.G., and Ribelayga, C.P. (2016). Direct evidence for daily plasticity of electrical coupling between rod photoreceptors in the mammalian retina. J. Neurosci. 36, 178–184.

Kanjhan, R., and Sivyer, B. (2010). Two types of ON direction-selective ganglion cells in rabbit retina. Neurosci. Lett. 483, 105–109.

Kay, J.N., De la Huerta, I., Kim, I.J., Zhang, Y., Yamagata, M., Chu, M.W., Meister, M., and Sanes, J.R. (2011). Retinal ganglion cells with distinct directional preferences differ in molecular identity, structure, and central projections. J. Neurosci. 31, 7753–7762.

Kim, I.J., Zhang, Y., Meister, M., and Sanes, J.R. (2010). Laminar restriction of retinal ganglion cell dendrites and axons: subtype-specific developmental patterns revealed with transgenic markers. J. Neurosci. 30, 1452–1462.

Kim, I.J., Zhang, Y., Yamagata, M., Meister, M., and Sanes, J.R. (2008). Molecular identification of a retinal cell type that responds to upward motion. Nature 452, 478–482.

Kuffler, S.W. (1953). Discharge patterns and functional organization of mammalian retina. J. Neurophysiol. 16, 37–68.

Lasater, E.M. (1987). Retinal horizontal cell gap junctional conductance is modulated by dopamine through a cyclic AMP-dependent protein kinase. Proc. Natl. Acad. Sci. USA 84, 7319–7323.

Lee, S., Chen, L., Chen, M., Ye, M., Seal, R.P., and Zhou, Z.J. (2014). An unconventional glutamatergic circuit in the retina formed by vGluT3 amacrine cells. Neuron 84, 708–715.

Li, P.H., Gauthier, J.L., Schiff, M., Sher, A., Ahn, D., Field, G.D., Greschner, M., and Callaway, E.M. (2015). Anatomical identification of extracellularly recorded cells in large-scale multielectrode recordings. J. Neurosci. 35, 4663–4675.

Madisen, L., Zwingman, T.A., Sunkin, S.M., Oh, S.W., Zariwala, H.A., Gu, H., Ng, L.L., Palmiter, R.D., Hawrylycz, M.J., Jones, A.R., et al. (2010). A robust and high-throughput Cre reporting and characterization system for the whole mouse brain. Nat. Neurosci. 13, 133–140.

McMahon, D.G., Knapp, A.G., and Dowling, J.E. (1989). Horizontal cell gap junctions: Single-channel conductance and modulation by dopamine. Proc. Natl. Acad. Sci. USA 86, 7639–7643.

Naarendorp, F., Esdaille, T.M., Banden, S.M., Andrews-Labenski, J., Gross, O.P., and Pugh, E.N., Jr. (2010). Dark light, rod saturation, and the absolute and incremental sensitivity of mouse cone vision. J. Neurosci. 30, 12495–12507.

Nath, A., and Schwartz, G.W. (2017). Electrical synapses convey orientation selectivity in the mouse retina. Nat. Commun. 8, 2025.

Oyster, C.W. (1968). The analysis of image motion by the rabbit retina. J. Physiol. 199, 613–635.

Oyster, C.W., and Barlow, H.B. (1967). Direction-selective units in rabbit retina: Distribution of preferred directions. Science 155, 841–842.

Pan, F., Toychiev, A., Zhang, Y., Atlasz, T., Ramakrishnan, H., Roy, K., Volgyi, B., Akopian, A., and Bloomfield, S.A. (2016). Inhibitory masking controls the threshold sensitivity of retinal ganglion cells. J. Physiol. 594, 6679–6699.

Park, S.J., Borghuis, B.G., Rahmani, P., Zeng, Q., Kim, I.J., and Demb, J.B. (2015). Function and circuitry of VIP+ interneurons in the mouse retina. J. Neurosci. 35, 10685–10700.

Pearson, J.T., and Kerschensteiner, D. (2015). Ambient illumination switches contrast preference of specific retinal processing streams. J. Neurophysiol. 114, 540–550.

Pei, Z., Chen, Q., Koren, D., Giammarinaro, B., Acaron Ledesma, H., and Wei, W. (2015). Conditional knock-out of vesicular GABA transporter gene from Starburst amacrine cells reveals the contributions of multiple synaptic mechanisms underlying direction selectivity in the retina. J. Neurosci. 35, 13219–13232.

Purushothaman, G., and Bradley, D.C. (2005). Neural population code for fine perceptual decisions in area MT. Nat. Neurosci. 8, 99–106.

Rivlin-Etzion, M., Zhou, K., Wei, W., Elstrott, J., Nguyen, P.L., Barres, B.A., Huberman, A.D., and Feller, M.B. (2011). Transgenic mice reveal unexpected diversity of on-off direction-selective retinal ganglion cell subtypes and brain structures involved in motion processing. J. Neurosci. 31, 8760–8769.

Rousso, D.L., Qiao, M., Kagan, R.D., Yamagata, M., Palmiter, R.D., and Sanes, J.R. (2016). Two pairs of ON and OFF retinal ganglion cells are defined by intersectional patterns of transcription factor expression. Cell Rep. 15, 1930–1944.

Sabbah, S., Gemmer, J.A., Bhatia-Lin, A., Manoff, G., Castro, G., Siegel, J.K., Jeffery, N., and Berson, D.M. (2017). A retinal code for motion along the gravitational and body axes. Nature 22, 492–497.

Salinas, E., and Abbott, L.F. (1994). Vector reconstruction from firing rates. J. Comput. Neurosci. 1, 89–107.

Schubert, T., Maxeiner, S., Kruger, O., Willecke, K., and Weiler, R. (2005). Connexin45 mediates gap junctional coupling of bistratified ganglion cells in the mouse retina. J. Comp. Neurol. 490, 29–39.

Seung, H.S., and Sompolinsky, H. (1993). Simple models for reading neuronal population codes. Proc. Natl. Acad. Sci. USA 90, 10749–10753.

Silverman, B.W. (1981). Using kernel density estimates to investigate multimodality. J. R. Stat. Soc. Series B Stat. Methodol. 43, 97–99.

Simpson, J.I. (1984). The accessory optic system. Annu. Rev. Neurosci. 7, 13–41.

Sivyer, B., van Wyk, M., Vaney, D.I., and Taylor, W.R. (2010). Synaptic inputs and timing underlying the velocity tuning of direction-selective ganglion cells in rabbit retina. J. Physiol. 588, 3243–3253.

Sohl, G., Maxeiner, S., and Willecke, K. (2005). Expression and functions of neuronal gap junctions. Nat. Rev. Neurosci. *6*, 191–200.

Sumbul, U., Song, S., McCulloch, K., Becker, M., Lin, B., Sanes, J.R., Masland, R.H., and Seung, H.S. (2014). A genetic and computational approach to structurally classify neuronal types. Nat. Commun. *5*, 3512.

Sun, L.O., Brady, C.M., Cahill, H., Al-Khindi, T., Sakuta, H., Dhande, O.S., Noda, M., Huberman, A.D., Nathans, J., and Kolodkin, A.L. (2015). Functional assembly of accessory optic system circuitry critical for compensatory eye movements. Neuron *86*, 971–984.

Taylor, W.R., and Vaney, D.I. (2002). Diverse synaptic mechanisms generate direction selectivity in the rabbit retina. J. Neurosci. *22*, 7712–7720.

Theunissen, F.E., and Miller, J.P. (1991). Representation of sensory information in the cricket cercal sensory system. II. Information theoretic calculation of system accuracy and optimal tuning-curve widths of four primary interneurons. J. Neurophysiol. *66*, 1690–1703.

Tikidji-Hamburyan, A., Reinhard, K., Seitter, H., Hovhannisyan, A., Procyk, C.A., Allen, A.E., Schenk, M., Lucas, R.J., and Munch, T.A. (2015). Retinal output changes qualitatively with every change in ambient illuminance. Nat. Neurosci. *18*, 66–74.

Trenholm, S., Johnson, K., Li, X., Smith, R.G., and Awatramani, G.B. (2011). Parallel mechanisms encode direction in the retina. Neuron *71*, 683–694.

Trenholm, S., McLaughlin, A.J., Schwab, D.J., and Awatramani, G.B. (2013). Dynamic tuning of electrical and chemical synaptic transmission in a network of motion coding retinal neurons. J. Neurosci. *33*, 14927–14938.

Trenholm, S., McLaughlin, A.J., Schwab, D.J., Turner, M.H., Smith, R.G., Rieke, F., and Awatramani, G.B. (2014). Nonlinear dendritic integration of electrical and chemical synaptic inputs drives fine-scale correlations. Nat. Neurosci. *17*, 1759–1766.

Trong, P.K., and Rieke, F. (2008). Origin of correlated activity between parasol retinal ganglion cells. Nat. Neurosci. *11*, 1343–1351.

Vaney, D.I. (1994). Territorial organization of direction-selective ganglion cells in rabbit retina. J. Neurosci. *14*, 6301–6316.

Vaney, D.I., Sivyer, B., and Taylor, W.R. (2012). Direction selectivity in the retina: Symmetry and asymmetry in structure and function. Nat. Rev. Neurosci. *13*, 194–208.

Wang, Y.V., Weick, M., and Demb, J.B. (2011). Spectral and temporal sensitivity of cone-mediated responses in mouse retinal ganglion cells. J. Neurosci. *31*, 7670–7681.

Wassle, H., Peichl, L., and Boycott, B.B. (1981). Dendritic territories of cat retinal ganglion cells. Nature *292*, 344–345.

Wei, W., Elstrott, J., and Feller, M.B. (2010). Two-photon targeted recording of GFP-expressing neurons for light responses and live-cell imaging in the mouse retina. Nat. Protoc. *5*, 1347–1352.

Wyatt, H.J., and Daw, N.W. (1975). Directionally sensitive ganglion cells in the rabbit retina: Specificity for stimulus direction, size, and speed. J. Neurophysiol. *38*, 613–626.

Xin, D., and Bloomfield, S.A. (1999). Dark- and light-induced changes in coupling between horizontal cells in mammalian retina. J. Comp. Neurol. *405*, 75–87.

Yoshida, K., Watanabe, D., Ishikane, H., Tachibana, M., Pastan, I., and Nakanishi, S. (2001). A key role of starburst amacrine cells in originating retinal directional selectivity and optokinetic eye movement. Neuron *30*, 771–780.

Yu, W.Q., Grzywacz, N.M., Lee, E.J., and Field, G.D. (2017). Cell type-specific changes in retinal ganglion cell function induced by rod death and cone reorganization in rats. J. Neurophysiol. *118*, 434–454.

Zylberberg, J., Cafaro, J., Turner, M.H., Shea-Brown, E., and Rieke, F. (2016). Direction-selective circuits shape noise to ensure a precise population code. Neuron *89*, 369–383.

STAR★METHODS

KEY RESOURCES TABLE

REAGENT or RESOURCE	SOURCE	IDENTIFIER
Chemicals, Peptides, and Recombinant Proteins		
Tamoxifen	Sigma	CAS: 10540-29-1
Neurobiotin	Vector Laboratories	CAS: SP-1125-2
SR-95531	Tocris	CAS: 104104-50-9
Experimental Models: Organisms/Strains		
Mouse: wild-type (C57BL/6J)	The Jackson Laboratory	RRID: IMSR_JAX:000664
Mouse: Hb9::eGFP	Gift from Jeremy Kay (Duke University)	RRID: MGI_109160
Mouse: Ai9	The Jackson Laboratory	RRID: MGI_3809523
Mouse: Fstl4-CreER	Gift from Joshua Sanes (Harvard University)	MGI: 4437479
Mouse: Cx36-floxed	This paper	N/A
Mouse: FACx	This paper	N/A
Software and Algorithms		
MATLAB	MathWorks	http://www.mathworks.com/; RRID: SCR_01622
LABVIEW	National Instruments	http://www.ni.com; RRID: SCR_014325

CONTACT FOR REAGENT AND RESOURCE SHARING

Further information and requests for resources and reagents should be directed to and will be fulfilled by the Lead Contact, Greg D. Field (field@neuro.duke.edu).

EXPERIMENTAL MODEL AND SUBJECT DETAILS

Mice

All animals were healthy adults and housed in 12hr light-dark cycles, in groups up to 5 animals per cage. All procedures to maintain and use mice were in accordance with the Duke University Institutional Animal Care and Use Committee, University of Victoria's Animal Care Committee, and Harvard Medical School's Animal Care and Use Committee. Mice used in physiology experiments were 1 month – 11 months in age. 9 mice were males and 7 were females.

C57BL/6J (RRID: IMSR_JAX:000664) mice and Ai9 (RRID: MGI_3809523), a floxed-tdTomato (Cre reporter) mice (B6;129S6-$Gt(ROSA)26Sor^{tm9(CAG-tdTomato)Hze}$/J) were acquired from The Jackson Laboratory. Hb9::eGFP (RRID: MGI_109160) mice were acquired from Dr. Jeremy Kay at Duke University.

We generated the FACx mice by crossing the Fstl4-CreER mice and Ai9 mice and crossing their progeny with a previously unpublished Cx36-floxed (Cx36fl) line (see below). Fstl4-CreER mice were shown previously to exhibit expression of Cre in superior-preferring ON-OFF DSGCs following administration of tamoxifen (Kim et al., 2010). Ai9 mice express tdTomato in cells that express Cre (Madisen et al., 2010). Thus, in the FACx mice, activation of Cre via tamoxifen administration eliminated expression of Cx36 and induced expression of tdTomato (Figure S3L and S3M). Tamoxifen (100 μg, Sigma) was injected intraperitoneally into FACx mice at postnatal day 0 or day 1 (P0 or P1) to activate CreER.

To generate the Cx36fl mouse line, A 13kb genomic clone spanning exons 1 and 2 of Cx36 was isolated from a 129SV genomic phage library (Stratagene) using a 533 bp probe corresponding to the sequences encoding the cytoplasmic loop and carboxy-terminus of Cx36. Two fragments were generated by HindIII digestion and subcloned. The first fragment (∼1 kb) comprised the 5′ homology arm of the targeting construct, containing exon 1 and a portion of the flanking intron. The second fragment (∼5 kb) contained the remaining portion of the intron and second exon. To produce the 3′ homology arm from the second fragment, a Pme1 site was introduced following the stop codon so a loxP site, with a diagnostic EcoR1 site, could be inserted. The 5′ and 3′ homology arms were then subcloned into a modified version of the targeting vector pDTA (gift of Frank Gertler) containing a floxed TK/neomycin selection cassette. J1 ES cells were electroporated as described before (Deans and Paul, 2001) and 183 neomycin-resistant clones selected. For the primary screen, a PCR amplicon was generated using one primer within the coding region of exon 2 and another downstream of the 3′ homology arm and digested with EcoR1. To verify proper recombination at the 5′ arm,

ES cell DNA was digested with EcoR1 and Southern blotted using a probe located upstream of the 5′ homology arm. Due to the presence of an EcoR1 site in the *neo* cassette, the wild-type band and KO displayed different size bands. To remove the selection cassette, two correctly targeted ES cell clones with good karyotypes were transfected with *cre* recombinase. 132 clones were screened by PCR for excision of the TK/Neomycin cassette (primers C and D) without excision of exon 2 (primers C and E) and 15 correctly recombined clones were identified. ES cells were injected into C57/BL6 blastocysts and highly chimeric pups were crossed with WT C57/BL6 to obtain floxed Cx36 (Cx36*fl*) heterozygotes. To produce a cone-specific Cx36 KO, a Cx36*fl* $^{+/-}$ line was crossed with transgenic animals expressing *cre* under control of S-opsin (BP) and M-opsin (RGP) promoters (Akimoto et al., 2004). BP-cre$^+$/Cx36*fl* $^{+/-}$ and RGP-cre$^+$/ Cx36*fl* $^{+/-}$ mice were then crossed to generate RGP/BP-Cre$^+$/Cx36*fl* $^{+/+}$ cone-specific KOs and littermate RGP/BP-cre$^+$/Cx36*fl* $^{+/-}$ and RGP/BP-cre$^+$/WT Cx36 controls. Detection of the RGP-Cre and BP-Cre transgenes was carried out using PCR primer F and G or F and H, respectively.

A: GCG GAG GGA GCA AAC GAG AAG (5′, in 2nd exon coding)
B: CAC CAG AAT GGG GCT TTT ATC ACT ACT G (3′, outside construct)
C: ATT CTT ACA TTG AGC TGG AC (5′ intron ahead of *neo* cassette)
D: CCT TGA GTG GTA CTG AAC TG (3′ intron after *neo* cassette)
E: GGG AGA AAT ATC CTC CAG G (3′, 3′ UTR after LoxP)
F: AAT GGG AAC AGT GGT GTG TG (5′, RGP promoter)
G: AGG AGG GTG CTG TAG GGA AG (5′, 5′ BP promoter)
H GAA CGA ACC TGG TCG AAA TC (3′, *cre*)

To validate the cre-dependence of Cx36 excision in conditions distinct from targeting RGCs, floxed Cx36 mice were crossed with an M- and S- cone opsin-*cre* transgenic lines (Akimoto et al., 2004), and immunoreactivity for Cx36 was compared with WT retinas. In a WT retina, anti-Cx36 antibody labeled numerous puncta (Figure S3I) located in both the inner and outer plexiform layers (IPL and OPL, respectively). This pattern of expression was not altered in retinas from animals homozygous for the floxed Cx36 allele in the absence of *cre* (data not shown). However, in the cone-specific Cx36KO retinas, OPL expression of Cx36 was dramatically lower than in the WT (Figure S3J), while IPL expression was unchanged. Double-labeling for Cx36 and the cone pedicle marker PNA (Figure S3K) revealed that the residual OPL Cx36 expression was proximal to the pedicles, likely originating in cone bipolar cells (Deans et al., 2002; Feigenspan et al., 2004; Feigenspan et al., 2001; Han and Massey, 2005) rather than photoreceptors. These results indicate this floxed Cx36 mouse line allows for cre-dependent knockout of Cx36.

METHOD DETAILS

Recording Procedures
Animals were dark-adapted overnight and euthanized by decapitation. Euthanasia and retinal dissections were performed with the assistance of infrared converters in a dark room. Effort was taken to eliminate sources of visible light during the dissection. Following euthanasia, the eyes were removed and hemisected under a dissection microscope with infrared converters. Dorsal peripheral retina was isolated and mounted on an array of extracellular microelectrodes with ganglion cell side down (Elstrott et al., 2008; Field et al., 2007; Yu et al., 2017). Dorsal retina was identified by observing the vasculature under IR illumination, which reveals a cross-like structure just ventral to the optic nerve head (Wei et al., 2010). Dorsal retina was used to measure responses from areas with the highest expression of middle-wavelength sensitive opsin in cone photoreceptors (Applebury et al., 2000). This facilitated the delivery of visual stimuli that drove rod-dominated and cone-dominates responses. The orientation of the dorsal-ventral axis in each recording was determined by observing the RGC EIs (Figure S1A). The axons of RGCs in the dorsal retina head in the ventral direction, and we observed the axons in the EIs. This information, combined with the eye (left or right) that was used in the dissection, allowed us to put the stimuli presented to the retina in visual coordinates (superior, inferior, posterior and anterior). The MEA consists of 519 electrodes with 30 μm spacing, covering a hexagonal region 450 μm on a side (Field et al., 2010; Frechette et al., 2005). While recording, the retina was perfused with Ames' solution (30-32°C) bubbled with 95% O_2 and 5% CO_2, pH 7.4.

Light Stimulation
Stimuli were created in MATLAB (Mathworks, Natick, MA) and generated with a gamma-corrected OLED microdisplay refreshing at 60.35 Hz (SVGA+XL Rev3, eMagin. Santa Clara, CA). The image was projected through the microscope objective (Nikon, CFI Super Fluor 4x) and focused through the retina onto the photoreceptor outer segments. The emission spectrum of each display primary was measured with a PR-701 spectra-radiometer (PhotoResearch) after passing through the optical elements between the display and the retina. Photon flux was measured at the focal plane of the MEA using a photodiode (UDT Instruments) and converted to photo-isomerizations per rod per second assuming a collecting area of 0.5 μm^2 (Field et al., 2009; Field and Rieke, 2002).

Light level was controlled by neutral density filter placed in the light path. Mean light levels used here spanned five orders of magnitude from 1 to 10000 R*/rod/s. All experiments began at the lowest mean light level and increased by factors of 10 or 100 between light levels. The retina was exposed to the new light level for at least five minutes before presenting a battery of stimuli (e.g., drifting gratings or moving bars). Previous studies suggested that the threshold for cone activation is ∼100 R*/rod/s, but rod-mediated

signals still dominate vision (Naarendorp et al., 2010). Rod-mediated responses are saturated around 5000 R*/rod/s, above which the signaling is driven by cones (Wang et al., 2011). Thus, the light levels used here covered scotopic, mesopic, and photopic vision.

Three types of stimuli were used: (1) drifting gratings moving in 8 directions with speeds ranging from 24-2400 μm/s, at a spatial period of 960 μm (49.2° visual angle) and at 50% Michelson contrast; (2) moving bars traveling in either 8 or 12 directions, spanning a range of 5%–80% Weber contrast, at a speed of 960 μm/s and width of 480 μm (24.6° visual angle); (3) checkerboard binary white noise with 40 × 40 μm checker size, 60.35 Hz refreshing rate. Drifting gratings of different directions and speeds were presented in a pseudo-random order. Each grating was presented for 8 s with 2 s of gray screen between gratings. Each grating was presented 3-4 times. Moving bar stimuli were repeated 10 times, each bar presentation lasted between 1.6 and 2.4 s and bar directions (and contrasts) were presented in a psuedo-random order. For drifting gratings and moving bars, contrasts were held constant when comparing responses across light levels to isolate changes due to adaptation to the mean light level as opposed to contrast-dependent effects. Contrasts of the moving bars were only varied at low light level in experiments presented in Figure 5 to probe the contrast dependence of the null direction response.

Spike Sorting and EI Analysis

Recordings were analyzed offline to identify and sort the spikes of different cells, as described previously (Dabrowski et al., 2004; Field et al., 2007; Yu et al., 2017). Briefly, candidate spike events were detected using a threshold on each electrode, and voltage waveforms on the electrode and nearby electrodes around the time of the spike were extracted. Clusters of similar spike waveforms were identified as candidate neurons if they exhibited a refractory period (1.5 ms) with an estimate of < 10% contamination and consisted of more than 100 spikes (30 min recording time). Duplicate spike trains identified across different electrodes were identified by temporal cross-correlation and removed.

After the spikes from a given neuron were isolated on a source electrode, the average electrical activity in a time window from 1 ms before to 3 ms after the spike was calculated across the electrode array. Because the spiking activity of any given cell is largely independent of all other cells, the average electrical activity across the array reveals a unique electrical footprint for every cell (called an 'electrical image'), reflecting its position, extent of dendritic arbor and axon trajectory relative to the electrode array. Electrical images (EIs) are displayed as a dot pattern (Figure S1), where each dot represents the location of the electrode at which the signal from the neuron was detected and the diameter of the dot is proportional to the amplitude of the peak of the electrical waveform associated with a spike, collapsed over time (Field et al., 2009). The centers of mass (COM) of the EIs were compared to the locations of labeled cells (Figure S1) to estimate distances between genetically defined cell populations and functional cell population. COMs were estimated from a hexagonal ROI with a radius of 90 μm (3 electrodes). The center of the ROI was chosen to be the electrode with largest electrical activity amplitude. When the electrode with the largest signal from an RGC was located at the edge of the array, the ROI consisted exclusively of five electrodes at the array edge, flanking the electrode with the largest signal. Small displacements between RF locations and EI location could be induced by pressing the retina against the array MEA (Li et al., 2015). We estimated these distortions locally by comparing the EI positions and RF locations of non-DSGCs (ON and OFF brisk sustained and brisk transient cells), for whom the RFs could be well estimated from checkerboard noise. By measuring for each of these non-DSGCs the displacement between the RF center of mass and EI location, we produced a vector field of displacements across the MEA. Through linear regression, we fit a linear distortion map to this vector field. This distortion map was then used to shift DSGC EI positions (Figure 1H) to estimate their RF locations.

DSGC Classification

DSGCs were distinguished from other RGCs by fitting a two-Gaussian mixture model to the natural log of the vector sum magnitudes calculated from drifting gratings moving at 480 μm/s and 240 μm/s (Figure 1C). Both gratings had a spatial period of 960 μm. One Gaussian captured the DSGCs, the other captured non-DSGCs (magenta versus black in Figure 1C). The mixture model was fit to the log of the vector sum magnitudes because the distributions of points were approximately log normal, while in linear scale they are bounded to be greater than zero, causing the distributions to be skewed (Figure 1D).

To separate ON from ON-OFF DSGCs, principal components analysis (PCA) was applied to the speed tuning curves (estimated from drifting square wave gratings, 960 μm spatial period) to generate a representation of their shapes in two-dimensions (Figures 1E–1G). A two-Gaussian mixture model was fit to these data in the space defined by the first and third principal components with each Gaussian capturing ON and ON-OFF DSGCs respectively. The first and third principal components were used because they provided the largest separation between the two groups. In both classification steps (distinguishing non DSGCs from DSGCs and distinguishing ON from ON-OFF DSGCs), the analysis was performed separately in each retinal recording on the MEA.

Neurobiotin Labeling

Following 30-minute intracellular filling with Neurobiotin, retinas were fixed in 4% paraformaldehyde for 30 minutes and washed in 0.1X phosphate buffered saline (PBS), pH 7.4 for 15 minutes. Retinas were post-fixed overnight in a 30% sucrose, 0.1X PBS solution then washed in 1X PBS for 15 minutes. To visualize Neurobiotin, retinas were incubated in streptavidin-containing solutions (streptavidin-Cy3 or streptavidin-Alexa488 in 0.3% Triton in PBS). Following final washes in PBS, retinas were mounted in Fluoromount medium (Sigma-Aldrich). Coverslips were sealed for prolonged storage and slides were stored in dark at 4°C.

Images were collected using an Olympus confocal microscope with a 20x objective. Fluorophores (Ai9 and AlexaFluor 488) were excited with 554 nm and 488 nm lasers, respectively, and a pixel dwell time of 8.0 s/pixel. Image stacks were collected in 2 m Z-steps at a resolution of 0.828 m/pixel. For quantification, 10 planar images were Z projected (maximum intensity) and Gaussian filtered. Using ImageJ software, fixed-diameter circular ROIs were superimposed over Ai9$^+$ or GFP$^+$ somata and intensity values were recorded.

Immunohistochemistry

For immunohistochemical experiments (Figures S3I–S3K), eyes were enucleated and eyecups prepared in oxygenated Ames's medium under a dissection microscope (Deans et al., 2002). Unfixed eyecups were embedded in OCT and 12 μM cryosections were collected on Superfrost Plus^{TM} microscope slides (Fisher Scientific) and stored for further use at $-20°$C. Prior to labeling, sections were brought to room temperature then fixed in ice-cold methanol buffered with 10% MES, pH 7.4 for 20 s. Slides were then washed in PBS and blocked in PBS with 10% donkey serum and 0.2%Triton X-100 for 1 hr at room temperature before overnight incubation with anti-Cx36 antibody (1:1000, Chemicon) at 4°C. Slices were then washed in PBS and incubated in Cy3-conjugated goat anti-mouse secondary antibody (1:1500; Chemicon) for 1 hr at room temperature. Sections were examined with a Nikon E800 microscope equipped for epifluorescence or a Zeiss LSM 510 laser scanning confocal microscope.

Direction Tuning Estimation

The normalized spike count in each direction was calculated by dividing the average spike count in each direction by the maximum across all directions. The average spike count was baseline subtracted here, and the baseline activities were estimated either from one minute of spontaneous activity at the beginning of recording, or from activity during inter-stimulus intervals. The value of normalized spike count ranged from 0 to 1. The vector sum was calculated as the summation of these normalized response vectors. The direction selectivity index (DSI) was calculated as follows:

$$DSI = \frac{pref - null}{pref + null} \tag{1}$$

where $pref$ is the response in the stimulus direction closest to the preferred direction and $null$ is the response in the opposite stimulus direction. The preferred direction was obtained from the direction of the vector sum.

To estimate direction tuning width, tuning curves were fitted to a raised sinusoid function:

$$R(\theta) = R_{\max} \times [(0.5 + 0.5 \times \cos(\theta + \varphi))^\alpha \times \beta + (1 - \beta)] + R_{base} \tag{2}$$

where α sets the width of tuning curve, and β sets the null direction responses of tuning curve. Here we used the half-maximum width of direction modulated responses as direction tuning width, which is $2 \times \arccos(2^{(1-\alpha^{-1})} - 1)$.

The speed tuning was calculated by dividing the unnormalized vector sum in each speed by the maximum across speeds.

Cell selection

To identify superior-preferring ON-OFF DSGCs with the highest likelihood of having undergone cre-mediated excision of Cx36, we set two criteria. First, a tdTomato$^+$ cell was present within 50 μm of an identified superior-preferring ON-OFF DSGC location. Second, the superior-preferring ON-OFF DSGC did not exhibit bimodal peaks in the cross-correlogram with any other ON-OFF DSGC. To compute the cross-correlogram, we binned spike trains into 0.25 ms bin, and calculated the correlation coefficient as a function of time shift between two spike trains. When quantifying the proportion of neighboring pairs that are electrically coupled, we defined cells as neighbors if the distance between the EI centers of mass was < 150 μm. To identify bimodal structure in the cross-correlogram between two cells, three criteria were used: (1) the unimodal hypothesis was rejected by using a bootstrap algorithm (p < 0.05) (Carcieri et al., 2003; Silverman, 1981); (2) the peak location, defined by argmax of the cross correlogram, is between -2.5ms to 2.5ms. This constraint was added to exclude false positives. (3) the ratio calculated in Equation 3 is larger than 2.

$$ratio = \frac{\sum_{-3.5ms}^{-1ms} Q(\tau) + \sum_{1ms}^{3.5ms} Q(\tau)}{2 \times \min((Q * H)(\tau))} \tag{3}$$

where Q is the cross-correlation function between two cells after baseline subtraction, and H is a summation filter with a length of 2.5ms, convolved with Q. The convolution is run from -10 ms to 10 ms with zero padding. Criteria (3) ensures that the peaks observed within the expected time windows are robust over noise.

Superior-preferring ON-OFF DSGCs in FACx mice exhibited lower spike rates than in control animals. To test whether this difference could account for the reduction in observed coupling, we truncated the spike trains of superior-preferring ON-OFF DSGCs in WT mice to match the spike numbers to those observed in FACx mice. We recalculated the cross-correlation functions with these truncated spike trains and found that significant coupling (as judged by the three criteria above) persisted. This indicates that a lack of coupling in FACx mice could not be attributed to measuring fewer total spikes but resulted from fewer nearly-synchronous spikes.

Leaky Integrate-and-Fire Model

A leaky Integrate-and Fire model was used to analyze the joint effect of gap junction coupling and diminished effective inhibition on DSGC tuning curves. The excitatory and inhibitory synaptic conductances were simulated with the following empirical equation (Bekkers and Stevens, 1996).

$$G(t) = g_{max} \left[1 - \exp\left(-\frac{t - t_0}{\tau_1} \right) \right]^x \exp\left(-\frac{t - t_0}{\tau_2} \right) \tag{4}$$

g_{max} was modulated to change the amplitude of the conductance (Figure S5I, left), and t_0 was modulated to change the timing of the input conductance, which was determined by the direction and speed of a simulated moving bar (850 μm/s) and the locations of the simulated cells. All other parameters were fixed (τ_1 = 200 ms, τ_2 = 100 ms, x = 10) and estimated from a previous work (Figure 3C of (Zylberberg et al., 2016)). g_{max} of the excitatory conductance was set to be direction independent and g_{max} of the inhibitory conductance was direction tuned and generated from a raised sinusoid function (Figure S5I, right).

$$G_{exc}(\theta, t) = G(t) \tag{5}$$

$$G_{inh}(\theta, t) = A\{a_1 + b_1[0.5 + 0.5 * \cos(\theta + \varphi)]^\alpha\}G(t) \tag{6}$$

Where $a_1 = 1$, $b_1 = 2$, $\varphi = \pi/2$, $\alpha = 1$. The gain factor (A, Equation 6) on the inhibitory conductance was used to tune the amount of inhibition. When A = 1, the inhibitory conductance equals the excitatory conductance for preferred direction motion and is 3-fold greater than the excitatory conductance for null direction motion. From these conductances, voltage traces were generated with a leaky integrator.

$$C\frac{dV}{dt} = I_{synapse}(t) + I_{leaky}(t) + I_{gap}(t) \tag{7}$$

where $I_{synapse}(t) = G_{exc}(t)(V(t - \Delta t) - E_{exc}) + G_{inh}(t)(V(t - \Delta t) - E_{inh})$
$$I_{leaky}(t) = G_{leak}(V(t - \Delta t) - E_{leak})$$
$$I_{gap}(t) = \sum_{i=1}^{n} G_{gap}^{(i)} \left(V(t - \Delta t) - V^{(i)}(t - \Delta t) \right)$$

A 5 ms absolute refractory period and an exponentially decaying relative refractory period (4 mV amplitude, 8 ms tau) were included in this model. A semi-regular mosaic of superior-preferring DSGCs was simulated with density of 120 cells/mm^2 (Eglen, 2006). Within this mosaic, two cells were gap junction coupled if their distance was smaller than 150 μm (Figure S5K). $G_{gap}^{(i)}$ was set to 0.8 nS for coupled cells (Trong and Rieke, 2008) and 0 nS for uncoupled cells. The following parameters were used in the model: $C = 0.03\,nF$, $E_{exc} = 0\,mV$, $E_{inh} = -80\,mV$, $E_{leak} = -60\,mV$, $G_{leak} = 4\,nS$, $V_{thresh} = -50\,mV$.

Decoding Model

To simulate the motion detection and discrimination performance across populations of DSGCs, we modeled quartets of ON-OFF DSGCs. Their direction tuning was modeled with raised sinusoid functions (Equation 2), where the preferred direction φ was fixed to $[0, \pi/2, \pi, 3\pi/2]$ and R_{base} fixed to the background activity we measured from MEA recording. Responses of the quartet to bars moving in different directions were simulated with a Poisson noise model:

$$p_{poiss}(r \mid \theta) = \frac{R(\theta)^r e^{-R(\theta)}}{r!} \tag{8}$$

where $p_{poiss}(r \mid \theta)$ is the probability of generating r spikes when a stimulus θ is presented. The peak firing rates in our tuning curve model were estimated from DSGC responses under rod and cone light levels. The stimulus direction was estimated from a simulated response using a maximum-likelihood (ML) decoder:

$$\widehat{\theta} = \underset{\theta}{\text{argmax}}(L(r \mid \theta)) \tag{9}$$

where $L(r \mid \theta)$ is the likelihood of observing a population response r when presenting stimulus θ, assuming there is no noise correlation:

$$L(r \mid \theta) = \prod_{k=1}^{4} p(r_k \mid \theta) \tag{10}$$

The direction discrimination error was estimated by averaging $\mid \theta - \widehat{\theta} \mid$ across all stimulus directions.

For the motion detection task, we generated two simulated responses: one for a simulated moving bar, r_m, and one for simulated spontaneous activity, r_s. The probability of spiking for r_s was given by sampling from a Poisson distribution with a mean rate of 0.02 spikes/trial (R_{base}, Equation 2). The task was to correctly label which response was generated by motion and which by spontaneous activity. For both r_m and r_s, we calculated the likelihood ratio that the response came from a motion-generated stimulus versus spontaneous activity. This yielded two likelihood ratios, one for r_m, $(L_m = max_\theta\{L(r_m(\theta)\,|\,\theta_{motion})/L(r_m(\theta)\,|\,no\ motion)\})$ and one for r_s $(L_s = max_\theta\{L(r_s\,|\,\theta_{motion})/L(r_s\,|\,no\ motion)\}$. The maximum operation over θ maximizes the probability of detecting motion across all possible directions, θ. Next, L_m and L_s were compared by taking their ratio, because both values could either be larger or smaller than unity and the task was a two-alternative forced-choice: $C = L_m/L_s$. When $C > 1$, the probability that r_m came from the motion stimulus is higher than that for r_s and the two responses are correctly labeled. When $C < 1$, the probability that r_m came from spontaneous activity is higher than r_s and the two responses are incorrectly labeled.

$$C = \frac{L_m}{L_s} = \frac{max_\theta\{L(r_m(\theta)\,|\,\theta_{motion})/L(r_m(\theta)\,|\,no\ motion)\}}{max_\theta\{L(r_s\,|\,\theta_{motion})/L(r_s\,|\,no\ motion)\}} \qquad (11)$$

Normalized performance for the detection task (Figures 6D and 6E) was computed by normalizing the detection rates after accounting for a chance performance of 0.5. Normalized performance of discrimination task was computed by normalizing $\frac{\pi}{2} - error$, since the average chance error is $\frac{\pi}{2}$.

Parameters for the model of DSGCs under the cone regime were estimated from a 40% positive contrast bar (480 μm width and 1.44 mm/s speed) moving in 8 directions at 10,000 R*/rod/s. From these responses at the cone-mediated light level (Figure 6E), the mean estimated tuning width (α) = 1.8, prefer null difference (β) = 0.95, and the preferred direction response (R_{max}) = 7.7 spikes. These numbers were used to simulate the 'narrow' tuning curves under photopic conditions. For simulating the 'broad' tuning curve under photopic conditions (Figure 6E), the following parameters were assigned to 'broad' tuning curve(s): α = 0.8, β = 0.6, and R_{max} = 15.4. This R_{max} was two-fold greater than for the 'narrow' tuning curves to match the difference in R_{max} observed under scoptopic conditions (1 R*/rod/s). Under rod-mediated conditions (Figure 6D), the parameters used in the simulation were estimated from the same stimulus presented on a background of 1 R*/rod/s. 'Broad' tuning was estimated from superior-preferring DSGCs and the model parameters were α = 0.8, β = 0.6, and R_{max} = 3. 'Narrow' tuning was estimated from the other three DSGC types where α = 1.8, β = 0.95, and R_{max} = 1.5. All parameters were estimated from fits of Equation 2 to the mean direction tuning curves estimated from each DSGC population. An analysis of how detection and discrimination performance depend on α, β, and R_{max} (Equation 2) is provided in Figure S6.

For the analysis in Figure 6C, cone (right), β and R_{max} were set to 1 (unitless) and 7.7 spikes, respectively. For Figure 6C, rod (left), β and R_{max} were 1 (unitless) and 1.5 spikes, respectively. For both plots in Figure 6C, α was varied to change the tuning width.

QUANTIFICATION AND STATISTICAL ANALYSIS

Unless otherwise noted, population averages are expressed as mean ± SEM. The number of cells and retinas are indicated in the figure legends; n represents the number of cells used unless indicated otherwise. Each retina came from a different mouse. No methods were used to determine whether the data met the assumptions of the statistical approach. Student's t test was used to compare values under different conditions, and the differences were considered significant when $p \leq 0.05$.

DATA AND SOFTWARE AVAILABILITY

The data analysis is available on request from the Lead Contact.